Construction and Building Materials 515 (2026) 145470

Contents lists available at ScienceDirect

Construction and Building Materials

journal homepage: www.elsevier.com/locate/conbuildmat

Long-term creep behaviour of cross-laminated bamboo and timber under axial compression: Experimental and probabilistic modelling

Zeda Yang [a], Hanlin Wei [a,b,c], Vittoria Borghese [d], Marco Zucca [e], Flavio Stochino [e], Yan Xiao [a,f], Cristoforo Demartino [d,*]

[a] Zhejiang University - University of Illinois at Urbana-Champaign Institute, Haining 314400 Zhejiang, PR China
[b] College of Civil Engineering and Architecture, Zhejiang University, Hangzhou, 310058 Zhejiang, PR China
[c] Department of Structural and Geotechnical Engineering, Sapienza University of Rome, 00184 Rome, Italy
[d] Department of Architecture, Roma Tre University, Rome, Italy
[e] Department of Civil Environmental Engineering and Architecture, University of Cagliari, 09123 Cagliari, Italy
[f] Department of Civil and Environmental Engineering, University of Illinois at Urbana-Champaign, Urbana, IL 61801, USA

ARTICLE INFO

Keywords:
Cross-laminated timber (CLT)
Cross-laminated bamboo timber (CLBT)
Creep
Viscoelastic modelling
Axial compression

ABSTRACT

Creep in Cross-Laminated Timber (CLT) and Cross-Laminated Bamboo-Timber (CLBT) panels governs long-term serviceability and reliability, yet its coupling with hygrothermal actions remains insufficiently quantified. This study combines experiments and modelling to characterize the compressive creep behaviour of three panel types: conventional CLT, CLBT with thick-strip GluBam (CLBT1), and CLBT with thin-strip GluBam (CLBT2). Short-term compression tests established baseline mechanical properties, followed by 180-day sustained-loading tests under controlled stress levels. Ambient Temperature (T) and Relative Humidity (RH) were continuously monitored to assess mechano-sorptive contributions to time-dependent strains. Both CLBT variants exhibited higher load-bearing capacity and greater resistance to retarded viscoelastic deformation than CLT, but showed increased sensitivity to humidity-driven effects. Deterministic viscoelastic models and probabilistic formulations incorporating hygrothermal covariates were developed and calibrated against the full experimental dataset. The probabilistic models reproduced the dispersion of creep strains more accurately and yielded realistic long-term creep coefficients with predictive intervals, enabling risk-informed assessment. A finite element application demonstrates how the proposed framework can be integrated into structural analyses to predict the long-term response of bio-based laminated components. The results demonstrate that accurate prediction of creep in laminated bamboo-timber systems requires explicit treatment of hygrothermal effects and material variability. The proposed methodology supports performance-based design and the broader adoption of sustainable, bio-based laminated construction products.

1. Introduction

The global drive towards sustainable construction has intensified interest in bio-based structural materials, with mass timber systems, particularly cross-laminated timber (CLT), emerging as viable, low-carbon alternatives to steel and concrete [1,2]. These engineered wood products offer an interesting combination of high strength-to-weight ratios, potential for prefabrication, and the ability to store atmospheric carbon, making them integral to modern decarbonization strategies [3]. Following these advances, innovative hybrid systems that incorporate engineered bamboo, such as Glued-Laminated Bamboo (GluBam), are being developed to create high-performance Cross-Laminated Bamboo-Timber (CLBT) composites [4,5]. Despite their growing popularity and promising mechanical properties, a significant challenge remains in understanding and predicting their long-term performance under sustained loads.

The primary obstacle to the widespread structural use of these bio-based materials is their inherent time-dependent deformation [6], or creep [7,8], which can compromise long-term serviceability [9] and structural safety [10,11]. For vertical structural elements such as columns and walls in mid- to high-rise buildings, compressive creep is particularly critical [12]; excessive shortening can trigger load redistribution [13], damage to non-structural components, and even stability issues under sustained loading [14,15]. Because wood and bamboo are viscoelastic, they continue to deform even under service-level stresses, a phenomenon that must be accounted for in design [7,16–18].

---

* Corresponding author.

E-mail addresses: zeda.23@intl.zju.edu.cn (Z. Yang), hanlin.23@intl.zju.edu.cn (H. Wei), vittoria.borghese@uniroma3.it (V. Borghese), marco.zucca2@unica.it (M. Zucca), flavio.stochino@unica.it (F. Stochino), yanxiao@intl.zju.edu.cn (Y. Xiao), cristoforo.demartino@me.com (C. Demartino).

https://doi.org/10.1016/j.conbuildmat.2026.145470
Received 14 October 2025; Received in revised form 28 January 2026; Accepted 29 January 2026

Nomenclature

e	Actual vapour pressure (hPa)
e_s	Saturation vapour pressure (hPa)
E_e	Elastic modulus of Maxwell spring (MPa)
E_d	Elastic modulus of Kelvin–Voigt spring (MPa)
η_d	Viscosity of Kelvin–Voigt dashpot (MPa d)
η_v	Viscosity of Maxwell dashpot (MPa d)
σ_0	Applied stress (MPa)
J	Time-dependent creep compliance (1/GPa)
ε_e	Instantaneous elastic strain
ε_c	Time-dependent creep strain
ε_d	Delayed elastic strain
ε_v	Viscous strain
ε_{tot}	Total measured strain
t	Time (day)
T	Ambient temperature (°C)
AH	Absolute humidity (g/m^3)
RH	Relative humidity (%)
σ_b	Bending strength (MPa)
M_{cap}	Bending capacity of beam (kN m)
M_{max}	Maximum bending moment along the beam (kN m)
b, h	Beam width and height (mm)
L_b, L_c	Beam length and column length (mm)
$\boldsymbol{\Theta}_c$	Model parameter vector ($\boldsymbol{\Theta}_0, \boldsymbol{\Theta}_m$)
$\boldsymbol{\Theta}_0$	Parameter vector of Burgers model
$\boldsymbol{\Theta}_m$	Parameter vector of explanatory functions
$h_i(\mathbf{x})$	ith dimensionless explanatory function
θ_i	Parameter for ith explanatory function
$\gamma(\mathbf{x}, \Theta_c)$	Bias-correction term in probabilistic model
ε_N	Standard normal random variable
σ	Model standard deviation
μ	Mean value of random variable
P_f	Probability of failure
P_{surv}	Survival probability
β	Reliability index

Creep in lignocellulosic materials is a manifestation of the time-dependent rearrangement of the macromolecular components of the cell wall—cellulose, hemicellulose, and lignin. While crystalline cellulose fibrils provide elastic stiffness, the amorphous matrix of hemicellulose and lignin behaves as a viscoelastic polymer, exhibiting time-dependent compliance that is heavily influenced by moisture content and temperature. As a matter of fact, the complexity of creep in wood [19] and bamboo is amplified by their hygroscopic nature [20]. Beyond simple viscoelastic creep observed under constant hygrothermal conditions, these materials exhibit mechano-sorptive (MS) creep [20], where deformation is markedly accelerated by fluctuations in moisture content [21–23]. This MS effect, often dominant in real climates, arises from the interplay between mechanical stress and the molecular rearrangement that occurs during moisture adsorption and desorption cycles [24,25]; in bamboo, related moisture-driven mechanisms have been observed under desorption conditions [26]. Lignocellulosic materials, exhibit a complex behaviour under thermal exposure, governed by the interplay between its main structural components (cellulose, hemicelluloses, and lignin), and minor constituents such as extractives and tannins [27–30]. During heating, the progressive removal of bound water and the onset of pyrolytic reactions lead to a sequence of overlapping degradation stages [31]. Furthermore, the anisotropic and hierarchical microstructure of wood and bamboo introduces additional complexities [32]. Factors such as grain direction, density gradients (increasing given by knots, or decreasing due to biotic attack), the distribution of vascular bundles in bamboo, and the presence of earlywood/latewood zones in timber all contribute to the material's intricate creep behaviour [33–35].

To predict this time-dependent behaviour, researchers have employed a variety of modelling strategies. Deterministic rheological models, such as the Burgers, Kelvin–Voigt, and Maxwell models, are widely used to represent the different phases of creep, including elastic, viscoelastic, and viscous deformation [36–39]. Power-law approaches, notably the Findley model, have also proved effective for long-term predictions [40–42]. Because long-duration testing is often impractical, accelerated characterization methods based on the Time-Temperature-Stress Superposition Principle (TTSSP) and the Stepped Isothermal Method (SIM) have been developed to extrapolate long-term performance from short-term experiments [43–46]. These models have been applied to a range of wood and bamboo products, including solid wood [47–49], Laminated Veneer Lumber (LVL) [50], Glulam [51–53], and various Wood-Plastic Composites (WPCs) [54–56].

However, a critical limitation of these deterministic approaches is their inability to account for the significant inherent variability of bio-based materials and the stochastic nature of surrounding hygrothermal conditions [57–63]. Material mechanical and physical properties (such as density, stiffness, and strength) may vary considerably even within the same species, and hygrothermal loads are inherently random. Consequently, a probabilistic modelling framework is essential for conducting realistic reliability analyses and developing performance-based design standards [64,65]. While advanced concepts such as fractional calculus for viscoelastic modelling [66,67] and Bayesian inference for parameter calibration [68] are being developed, their application has been hampered by a lack of high-quality, long-term experimental data, especially for novel hybrid systems like CLBT. There is a clear knowledge gap concerning the comparative long-term compressive performance of CLT and CLBT, and a need for validated probabilistic models that can capture their behaviour under coupled hygro-thermo-mechanical loading.

Therefore, this study presents an integrated experimental and modelling framework to investigate the long-term compressive creep behaviour of conventional CLT and two novel CLBT configurations. The research aims to address the aforementioned knowledge gaps by: ((i) conducting a comprehensive experimental campaign involving short-term mechanical tests and 180-day sustained compression tests under continuously monitored hygrothermal conditions; (*ii*) using the experimental database to develop and calibrate both deterministic and probabilistic creep models that explicitly account for material variability and the coupled effects of temperature and humidity; and (*iii*) demonstrating the application of the calibrated models in a finite element analysis to predict the time-dependent response of a structural system. The outcomes provide new insights into the serviceability performance of cross-laminated bio-composites and establish a robust basis for the reliability-based design of sustainable bamboo-timber hybrid structures.

The paper is organized as follows. Section 2 details the materials, specimen preparation, and experimental methodologies adopted in this study. The section describes the configuration of both the quasi-static compression tests (Section 2.2.1) and the long-term creep experiments (Section 2.2.2), including instrumentation, loading protocols, and hygrothermal monitoring. The test matrix summarizing all specimens and loading conditions is provided in Section 2.2.3. The section further introduces the framework for developing probabilistic model, including the formulation of the baseline deterministic model (Section 2.3.1), the general structure of the proposed probabilistic model (Section 2.3.2), and the procedure for model calibration and simplification (Section 2.3.3). Section 3 presents the experimental results, starting with the mechanical characterization under short-term loading (Section 3.1), followed by the time-dependent deformation behaviour observed during the 180-day creep campaign (Section 3.2). The influence of temperature and relative humidity variations on the creep

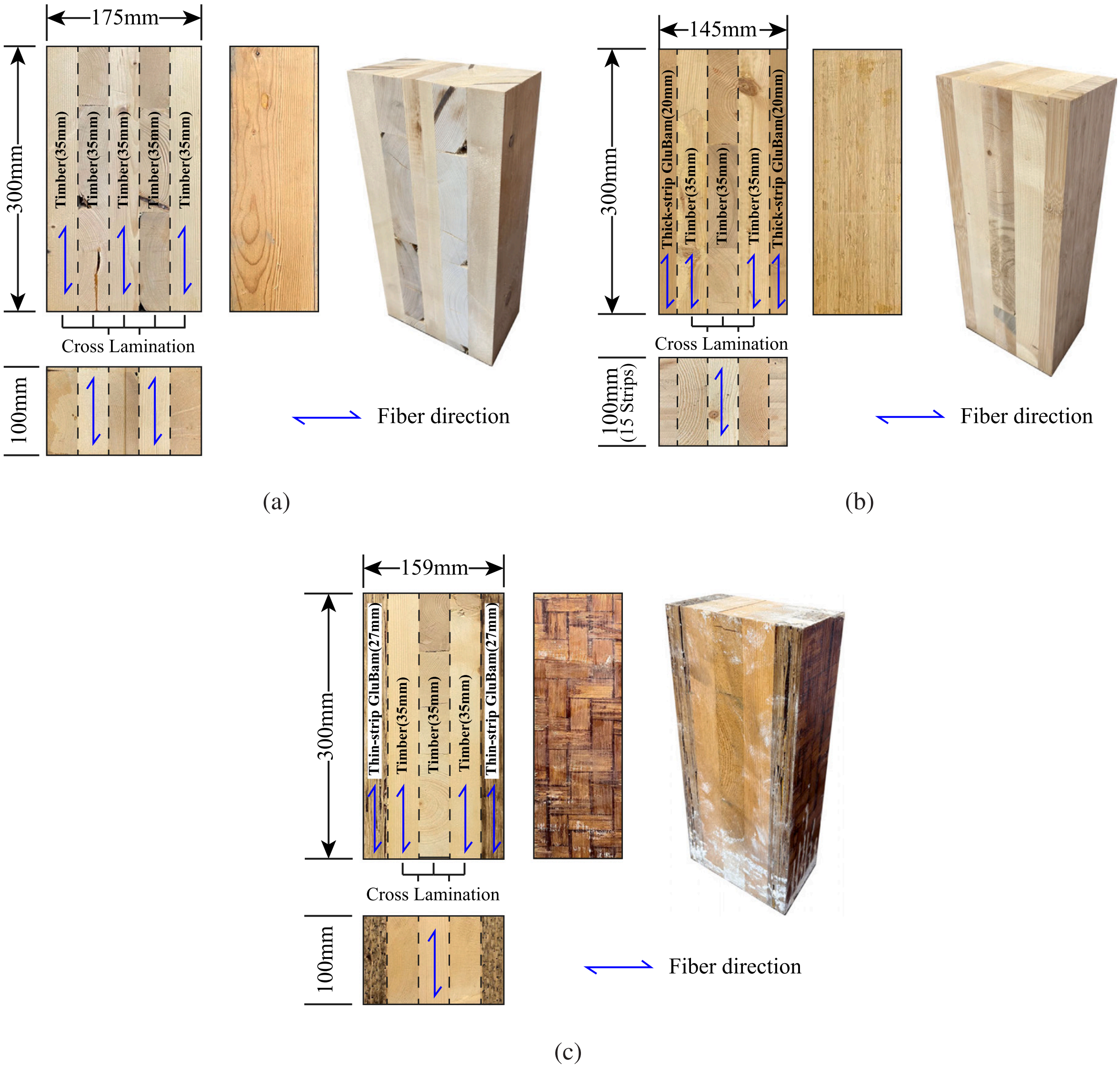

Fig. 1. Experimental specimens with (a) CLT, (b) CLBT1, and (c) CLBT2. For each specimen, a set of three orthogonal views and a perspective photograph are provided. In the three-view drawings, the upper-left image represents the front view, the upper-right image represents the side view, and the lower-left image represents the top view.

response is analysed in Section 3.2.2. Section 4 calibrates the deterministic and probabilistic creep models that account for material variability and hygrothermal effects, and presents the results of model selection and parameter uncertainty quantification. The predictive capability of the calibrated models is then demonstrated in a finite element analysis of a representative beam–column frame system in Section 5, providing insights into the time-dependent performance at the structural scale. Section 6 summarizes the main findings, discusses their implications for the design of cross-laminated bamboo–timber systems, and outlines directions for future research.

2. Materials and methods

2.1. Specimens: Preparation and characteristics

All specimens examined in this study were manufactured via a glued lamination process using structural-grade timber and bamboo elements. The timber lamellae were sourced from Pinus spp. (SPF: Spruce-Pine-Fir), a softwood widely employed in structural engineered wood applications. The bamboo lamellae were prepared from longitudinal splits of *Phyllostachys edulis* (Moso bamboo), which were processed into rectangular thick strips (5–8 mm thick, 25 mm wide) for CLBT1 and thin strips (1–3 mm thick, 20 mm wide) for CLBT2. Prior to bonding, the strips were kiln-dried to a target moisture content of 10 ± 2%. The dried strips were edge-glued along their longitudinal direction to form unidirectional veneer panels. These veneers were then arranged either in parallel along the grain direction for CLBT1 or in a cross-laminated configuration with a longitudinal-to-transverse orientation ratio of approximately 5:1 for CLBT2. The assembled layups were laminated using a phenol–formaldehyde (PF) resin under a hot-pressing temperature of 150 °C and a pressure of 6–8 MPa for approximately 15 min. After pressing, the laminated panels were conditioned at 20 ± 2 °C and 60 ± 5% RH for about five days to allow full adhesive curing and moisture equilibration. Three types of cross-laminated configurations were fabricated with careful control of fibre orientation, adhesive bonding, and geometric dimensions to ensure consistency across all specimens. Fig. 1 illustrates schematic diagrams and photographs of the three specimen types, including their cross-sectional configurations, dimensions, and grain orientation.

The CLT specimens (Fig. 1(a)) are composed entirely of timber lamellae arranged in a five-layer symmetric layup. Layers 1, 3, and 5

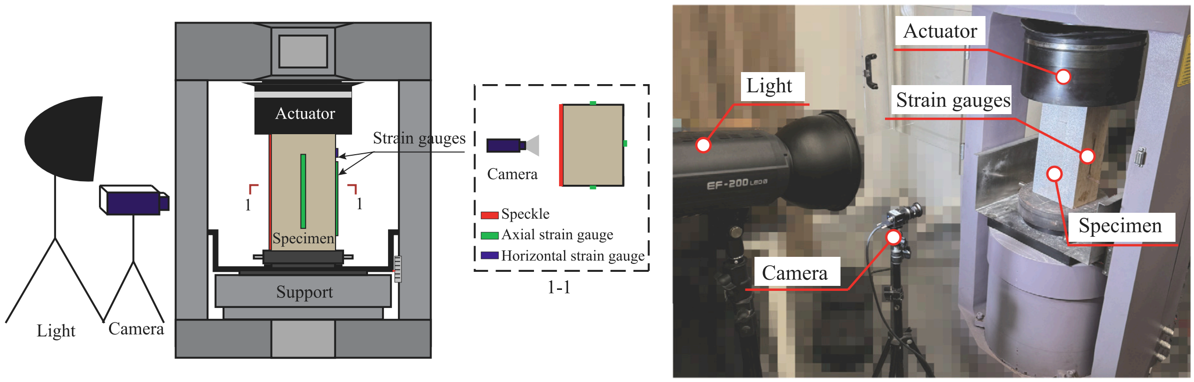

(a)

(b)

Fig. 2. Experimental setup for quasi-static compression tests: (a) schematic illustration highlighting the specimen placement, strain gauge locations, and digital image correlation (DIC) camera configuration; (b) photograph of the actual test arrangement, detailing the positions of actuator, specimen, strain gauges, camera, and lighting system used during testing.

are oriented longitudinally, while layers 2 and 4 are oriented transversely, perpendicular to the grain direction of the outer layers. Each lamella has a nominal thickness of 35 mm, resulting in a total cross-sectional size of 175 mm × 100 mm.

The CLBT1 specimens (Fig. 1(b)) featured a five-layer hybrid layup combining timber and bamboo components. The core comprises three timber lamellae, each 35 mm thick. The middle lamella is oriented perpendicular to the loading direction, whereas the adjacent layers are aligned longitudinally, parallel to the load axis. On both sides of the timber core, thick-strip GluBam lamellae (20 mm thick) made of thick bamboo strips are adhesively bonded. The cross-section of the CLBT1 specimen is 159 mm × 100 mm.

The CLBT2 specimens (Fig. 1(c)) adopted a similar five-layer configuration with a timber core and bamboo outer layers. The core includes three timber lamellae, each 35 mm thick, with the middle lamella oriented perpendicular to the loading direction. The outermost lamellae are thin-strip GluBam lamellae, each 27 mm thick, made of thin bamboo strips 2–3 mm in thickness. The final cross-section of the CLBT2 specimen is 145 mm × 100 mm.

2.2. *Test setup and measurements*

2.2.1. *Quasi-static compressive tests*

The primary objective of the quasi-static compression tests was to characterize the compressive mechanical behaviour of the CLT and CLBT specimens considered in this study. The testing procedures were carried out in accordance with GB/T 50329-2012 *Standards for Test Methods of Timber Structures* [69]. Specimens were precisely machined from the manufactured CLT, CLBT1, and CLBT2 wall components, with their dimensions and cross-sectional configurations shown in Fig. 1.

The experimental setup for the quasi-static tests is shown in Fig. 2. All specimens were tested on an HCT206E servo-controlled hydraulic-electric hybrid testing machine with a maximum load capacity of 2000 kN. Before testing, specimens were carefully aligned to minimize loading eccentricity. Each specimen underwent three preloading cycles under displacement control at a rate of 1.0 mm/min to eliminate mechanical slack and ensure uniform contact. The preloading was applied up to a target level of approximately 10% of the peak load (determined from preliminary tests on each configuration) and unloaded to 0.5 kN, followed by monotonic loading under displacement control at a constant rate of 0.9 mm/min in accordance with the standard procedure [69].

As illustrated in Fig. 2(a), four strain gauges and a Digital Image Correlation (DIC) system were installed. Three axial gauges were attached to the two side faces and the back face, respectively, to capture axial strain; the readings from these three gauges were averaged to obtain the nominal axial strain. One transverse gauge was installed on the back face to measure transverse strain. The strain data were recorded at a sampling frequency of 3 Hz. For full-field strain measurement, the front face of each specimen (showing the cross-laminated layers) was spray-painted with a speckle pattern and monitored with a digital image correlation (DIC) system. A high-resolution camera (Basler: 4096 × 3072 pixels, equipped with a 25 mm lens and an f/2.8 aperture) continuously acquired images at a frequency of 3 Hz throughout the loading process.

The compressive stress σ_c was calculated as the ratio of the applied load F to the gross cross-sectional area of the specimen A. Accordingly, the ultimate compressive strength σ_{cu} was defined as the stress corresponding to the maximum recorded load $F_{\max}$:

$$\sigma_{cu} = \frac{F_{\max}}{A} \tag{1}$$

The stress–strain relationship was fitted using a bilinear relationship as

$$\sigma_{\mathrm{c}}(\varepsilon_{\mathrm{s}}) = \begin{cases} E \cdot \varepsilon_{\mathrm{s}} & 0 \le \varepsilon_{\mathrm{s}} \le \varepsilon_{\mathrm{ce}} \\ E \cdot \varepsilon_{\mathrm{ce}} + E_s \cdot (\varepsilon_{\mathrm{s}} - \varepsilon_{\mathrm{ce}}) & \varepsilon_{\mathrm{ce}} \le \varepsilon_{\mathrm{s}} \le \varepsilon_{\mathrm{cu}} \end{cases} \tag{2}$$

where ε_{s} denotes the axial strain in the quasi-static test, and σ_{c} is the corresponding axial compressive stress. The parameter E represents the initial elastic modulus, calculated as the slope between 20% and 40% of the ultimate compressive strength (σ_{cu}) [70]. The yield strain, $\varepsilon_{\mathrm{ce}}$, is defined as the strain at the intersection of the stress–strain curve and a line parallel to the elastic slope E offset by 0.1% strain (i.e., the 0.1% offset method, referring to existing code and literature [70,71]). E_s represents the secondary (or hardening) modulus, calculated as the slope of the line connecting the yield point and the peak stress point.

2.2.2. *Creep compressive tests*

Long-term compressive creep tests were conducted to evaluate the time-dependent deformation of CLT, CLBT1, and CLBT2 specimens under sustained axial compression. The experimental procedure followed the guidelines of GB/T 50329-2012 *Standards for Test Methods of Timber Structures* [69]. All tests were performed in the Structural Engineering Laboratory at the Zhejiang University-University of Illinois at Urbana-Champaign Institute (ZJUI) in Haining, China, from December 2024 to May 2025.

Fig. 3 illustrates the test setup for the long-term creep experiments. Two custom-designed steel loading frames were constructed, each comprising three independent loading units. Within each unit, compressive force was applied using three calibrated springs. The initial deformation of the springs was preset with a hydraulic jack, and the applied load was monitored in real time with a mechanical force-ring gauge

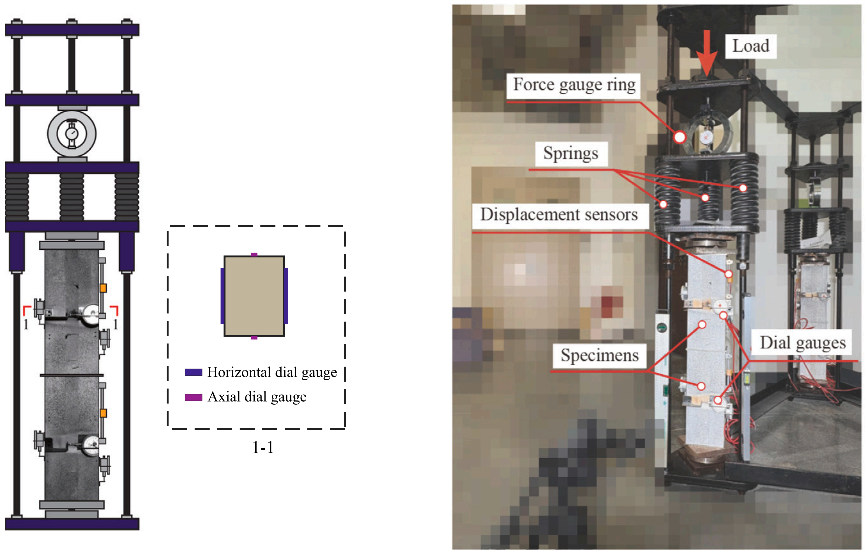

(a) (b)

Fig. 3. Creep test setup: (a) schematic showing the loading unit, and instrumentation; (b) photo of the experimental configuration including springs, force gauge ring, and specimen instrumentation.

mounted in each unit. Two vertically aligned specimens of the same material were installed in each unit, separated by a rigid steel plate. Both ends of the specimen assembly were supported by pin supports to ensure uniform load transfer and reduce boundary constraints.

The loading system was assembled from the bottom-up. Initial zero/baseline readings were recorded with dial gauges prior to loading. Compressive force was then introduced by adjusting a jack positioned at the top of each unit until the desired level was reached, as indicated by the mechanical force-ring gauge. Once the target load was reached, bolts were tightened to maintain the spring deformation. Surface displacement measurements were obtained using four dial gauges per specimen: two installed vertically on the side faces to monitor axial deformation, and two positioned horizontally on the front and back faces to capture transverse (horizontal) deformation. Since the dial gauges record displacement, readings were converted to engineering strain as $\varepsilon_{\mathrm{tot}} = \frac{\Delta L}{L_0}$, where $\varepsilon_{\mathrm{tot}}$ is the measured engineering strain; ΔL is the measured displacement from the dial gauge; L_0 is the gauge length between the two contact points. The exact locations of the measurement points are illustrated in Fig. 3(a).

With the two loading frames, a total of 21 specimens were tested. Among these, 12 specimens were assigned to the creep testing groups, organized into six groups with two specimens per group. The sample size for the loaded groups was constrained by the capacity of the loading apparatus; therefore, priority was given to covering a broader parameter space (three materials and two stress levels) to support robust model calibration. The creep groups covered two load levels (15% and 30% of the average compressive strength obtained from the static tests) for each of the three materials. In addition, 9 specimens served as the control group, consisting of three unstressed specimens for each material type, to isolate the hygrothermally induced strains under zero load.

For the creep group, all specimens were subjected to axial compression, and the measured strain in both the vertical and horizontal directions was considered to consist of three components [72]

$$\varepsilon_{\mathrm{tot}} = \varepsilon_{\mathrm{e}} + \varepsilon_{\mathrm{c}} + \varepsilon_{\mathrm{env}} \tag{3}$$

where $\varepsilon_{\mathrm{tot}}$ is the total measured strain from the strain gauges at time t; ε_{e} is the instantaneous elastic strain, measured immediately after loading in the creep groups; ε_{c} is the time-dependent net creep strain that develops under sustained load, and $\varepsilon_{\mathrm{env}}$ denotes the hygrothermally induced strain arising from thermal and moisture variations. The hygrothermally induced strain was measured as the strain data in control groups, where no external creep load was applied.

In this study, the creep strain is defined as the superposition of the instantaneous elastic strain (ε_{e}) and the time-dependent net creep strain (ε_{c}). Consequently, the creep strain was isolated by subtracting the hygrothermal component from the total measured strain, calculated as $\varepsilon = \varepsilon_{\mathrm{tot}} - \varepsilon_{\mathrm{env}}$. The resulting strains are denoted as ε_{V} for the vertical direction (parallel to loading direction) and ε_{H} for the horizontal direction (perpendicular to loading direction).

Continuous monitoring was conducted to capture the evolution of strain and hygrothermal conditions during the creep tests. Measurements included: (*i*) applied load, recorded by the mechanical force-ring gauges of the loading frames; (*ii*) axial and circumferential (horizontal) displacements, obtained from dial gauges mounted on both creep and control group specimens; (*iii*) time in days (t), ambient Temperature (T) and Relative Humidity (RH), monitored by digital sensors. Data were collected four times per day during the first 30 days, twice daily from day 30 to day 60, and once daily from day 60 to day 180.

2.2.3. *Test matrix*

Table 1 summarizes the specimens and loading regimes used in the quasi-static and long-term creep programmes. In total, 36 prismatic specimens were tested across three material systems (CLT, CLBT1, CLBT2): 15 for quasi-static characterization (5 per material) and 21 for creep, including loaded series and unloaded hygrothermal controls. The specimen geometry was identical across all groups (Fig. 1), ensuring direct comparability between short-term mechanical response and time-dependent deformation. For the creep series, target loads were set to 15% and 30% of the mean compressive strength, obtained from preliminary monotonic tests for each material. The specimen IDs encode both material and test regime: `CLT`, `CLBT1`, and `CLBT2` denote the material; the suffix `-S` indicates quasi-static tests, `-C15`/`-C30` indicate sustained-load creep at 15%/30% stress levels, and `-C0` marks unloaded hygrothermal controls.

2.3. *Deterministic and probabilistic predictive models*

2.3.1. *Deterministic model*

The Burgers model was adopted to characterize the axial compressive creep behaviour of CLT and CLBT. As illustrated in Fig. 4, this

Table 1
Test matrix for the quasi-static and long-term creep programmes.

Quasi-static programme				Creep programme			
ID	Stress level (%)	Load (kN)	Number	ID	Stress level (%)	Load (kN)	Number
CLT-S	–	–	5	CLT-C30	30	112.18	2
CLBT1-S	–	–	5	CLBT1-C30	30	99.34	2
CLBT2-S	–	–	5	CLBT2-C30	30	139.13	2
				CLT-C15	15	56.00	2
				CLBT1-C15	15	49.63	2
				CLBT2-C15	15	69.64	2
				CLT-C0	0	0.00	3
				CLBT1-C0	0	0.00	3
				CLBT2-C0	0	0.00	3

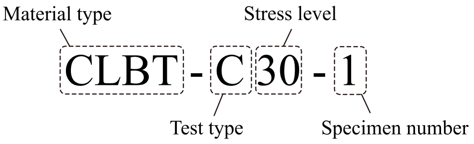

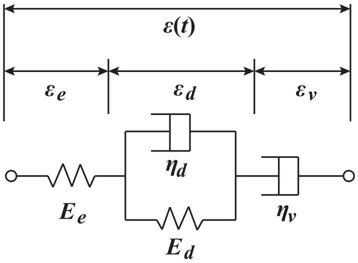

Fig. 4. Schematic representation of the Burgers model, combining a Maxwell element (spring E_e in series with dashpot η_v) and a Kelvin-Voigt element (spring E_d in parallel with dashpot η_d) to represent the total strain $\varepsilon(t) = \varepsilon_\mathrm{e} + \varepsilon_\mathrm{d} + \varepsilon_\mathrm{v}$.

model combines a Maxwell element (comprising an elastic spring (E_e) in series with a viscous dashpot (η_v)) with a Kelvin-Voigt element (consisting of a spring (E_d) and a dashpot (η_d) arranged in parallel). This configuration enables the model to represent three distinct creep components under sustained loading: the instantaneous elastic strain ε_e, the delayed elastic strain ε_d, and the viscous strain ε_v. The constitutive equation of the Burgers model under a constant applied stress σ_0 is expressed as [73]

$$\varepsilon = \varepsilon_\mathrm{e} + \varepsilon_\mathrm{c} = \varepsilon_\mathrm{e} + \left(\varepsilon_\mathrm{d} + \varepsilon_\mathrm{v}\right) = \frac{\sigma_0}{E_\mathrm{e}} + \left[\frac{\sigma_0}{E_\mathrm{d}}\left(1 - e^{-\frac{E_\mathrm{d}}{\eta_\mathrm{d}}t}\right) + \frac{\sigma_0}{\eta_\mathrm{v}}t\right], \tag{4}$$

where, E_e is the elastic modulus of the Maxwell spring, E_d is the elastic modulus of the Kelvin-Voigt spring, η_v is the viscosity of the Maxwell dashpot, η_d is the viscosity of the Kelvin-Voigt dashpot, and t is time. The first term σ_0/E_e represents the instantaneous elastic deformation occurring immediately after loading, the second term $\sigma_0/E_\mathrm{d}\left[1 - e^{-E_\mathrm{d}t/\eta_\mathrm{d}}\right]$ describes the retarded elastic deformation that develops asymptotically with time, and the third term $(\sigma_0/\eta_\mathrm{v})t$ accounts for the permanent viscous deformation that increases linearly with time.

In this study, two load levels corresponding to 15% and 30% of the statically determined ultimate compressive strength are applied in the creep tests (see Section 2.2.3). To allow for joint calibration of the Burgers model parameters across different stress levels, the constitutive equation was normalized by the applied stress σ_0 (in MPa). Accordingly, the creep behaviour was expressed in terms of the creep compliance function $J(t)$, which describes the time-dependent strain response of the material under a unit constant stress [74]

$$J = \frac{\varepsilon(t)}{\sigma_0} = \frac{1}{E_\mathrm{e}} + \frac{1}{E_\mathrm{d}}\left[1 - e^{-\frac{E_\mathrm{d}}{\eta_\mathrm{d}}t}\right] + \frac{t}{\eta_\mathrm{v}}. \tag{5}$$

In this normalized form, the model is independent of the magnitude of the applied stress, which enables the compliance curves at 15% and 30% can be fitted jointly.

The four parameters to be identified (E_e, E_d, η_d, η_v) were calibrated by fitting Eq. (5) simultaneously to all tests for a given material. Parameter identification used nonlinear least-squares regression with the compliance data from all specimens of each material. The fitting was implemented in Python with the `curve_fit` routine from the `scipy.optimize` package, which minimizes the squared error between the measured compliance $J(t)$ and the model prediction. Initial estimates for the four parameters in Eq. (5) were selected based on the instantaneous, delayed, and long-term slopes of the experimental curves, and both lower and upper bounds were imposed to ensure numerical stability and physical admissibility ($10^2 \leq E_\mathrm{e}, E_\mathrm{d}, \eta_\mathrm{d}$, $10^3 \leq \eta_\mathrm{v}$; $E_\mathrm{e}, E_\mathrm{d} \leq 10^6$, $\eta_\mathrm{d} \leq 10^8$, $\eta_\mathrm{v} \leq 10^9$).

2.3.2. Probabilistic models

For developing the probabilistic model, Absolute Humidity (AH) is required as an input parameter. Since the experimental records provide RH, a conversion is necessary. AH is defined as the mass of water vapour per unit volume of air, expressed in g/m^3, while RH represents the ratio between the actual and the maximum possible water vapour content at a given temperature. The conversion can be performed using the following relationship

$$AH = \frac{2.1674\,e}{273.15 + T} \times 100, \tag{6}$$

where $e = (RH/100) \cdot e_\mathrm{s}(T)$ is the actual vapour pressure (hPa), RH is the RH in percent, and $e_\mathrm{s}(T)$ is the saturation vapour pressure at temperature T (°C). The saturation vapour pressure is approximated by the Magnus formula

$$e_\mathrm{s}(T) = 6.112\,\exp\left(\frac{17.67\,T}{T + 243.5}\right). \tag{7}$$

Following the framework proposed by Gardoni et al. [64], the creep compliance, $J(\mathbf{x}, \boldsymbol{\Theta}_c, \sigma)$, is modelled as a deterministic mean function with a stochastic error term. To better satisfy the statistical assumptions of homoskedasticity, normality, and additivity [68], a transformation $T[\cdot]$ is applied. This leads to the general model form

$$T[J(\mathbf{x}, \boldsymbol{\Theta}_c, \sigma)] = T[\hat{J}(\mathbf{x})] + \gamma(\mathbf{x}, \boldsymbol{\Theta}_\mathrm{c}) + \sigma\varepsilon_\mathrm{N}, \tag{8}$$

where $T[\cdot]$ is a variance stabilizing transformation. In this study, the natural logarithm, $\ln(\cdot)$, was selected because creep compliance is strictly positive, spans a wide range, and exhibits scale-dependent variability; the logarithmic transformation stabilizes variance and yields residuals that are closer to normal in the transformed space, consistent with established probabilistic modelling practice [64]. $J(\mathbf{x}, \boldsymbol{\Theta}_c, \sigma)$ represents the probabilistic model for the predicted creep compliance, $\mathbf{x}$ denotes the vector of measurable explanatory variables (e.g., time t, temperature T, and absolute humidity AH), and $\boldsymbol{\Theta}_c$ represents the vector of unknown model parameters to be calibrated. $\hat{J}(\mathbf{x})$ is a deterministic median model, often derived from design codes or established physical laws; Since no such model exists for bamboo composites, this term is taken as zero; $\gamma(\mathbf{x}, \boldsymbol{\Theta}_c)$ is a predictive correction term to correct the bias between the prediction of $\hat{J}(\mathbf{x})$ and experimental observation. $\sigma\varepsilon_N$ represents the model error, where σ is the standard deviation and ε_N is a standard normal random variable, $\varepsilon_N \sim \mathcal{N}(0, 1)$.

With $\hat{J}(\mathbf{x}) = 0$, the mean of the log-transformed compliance is modelled entirely by the correction term $\gamma(\mathbf{x}, \boldsymbol{\Theta}_c)$. For this study, we propose a model that combines the intrinsic time-dependent behaviour using a Burgers formulation with the hygrothermal effects of temperature and humidity using a set of explanatory functions. The specific form for $\gamma(\mathbf{x}, \boldsymbol{\Theta}_c)$ is thus

$$\gamma(\mathbf{x}, \boldsymbol{\Theta}_c) = \ln\left[\frac{1}{E_e} + \frac{1}{E_d}\left(1 - e^{-\frac{E_d}{\eta_d}t}\right) + \frac{t}{\eta_v}\right] + \sum_{i=1}^{n} \theta_i h_i(\mathbf{x}), \tag{9}$$

where the terms $h_i(\mathbf{x})$ are dimensionless basis functions, chosen based on engineering principles to capture the influence of variables other than time. The total parameter vector $\boldsymbol{\Theta}_c$ is composed of two parts: $\boldsymbol{\Theta}_0 = (E_e, E_d, \eta_d, \eta_v)$ for the Burgers model components and $\boldsymbol{\Theta}_m = (\theta_1, \dots, \theta_n)$ for the selected explanatory functions.

To ensure that all explanatory variables are dimensionless and comparable, they are standardized before being used in the basis functions $h_i(\mathbf{x})$. For any raw variable X, its standardized form $S[X]$ is calculated as

$$S[X] = \frac{X - \mu_X}{\sigma_X}, \tag{10}$$

where μ_X is the sample mean of variable X; and σ_X is the standard deviation of variable X. This transformation creates variables with a zero mean and unit variance, allowing for a direct comparison of the calibrated coefficients θ_i to assess the relative importance of each explanatory variable.

2.3.3. Model selection for parsimony

A useful model must balance parsimony (using a minimal number of explanatory terms) with accuracy (maintaining a low model standard deviation, σ). To achieve this balance, a stepwise backward-elimination procedure, guided by Bayesian inference, is employed to reduce an initial full model with p candidate functions to a final, more efficient model with $n \le p$ functions.

The process begins with a full model incorporating all p candidate explanatory functions, $\boldsymbol{h}(\mathbf{x}) = [h_1(\mathbf{x}), \dots, h_p(\mathbf{x})]$. The elimination proceeds as follows:

1. Parameter Estimation: The posterior statistics (e.g., mean, standard deviation) of the model parameters, including the coefficients $\boldsymbol{\Theta}_m = (\theta_1, \dots, \theta_p)$ and the model deviation σ, are computed using a Bayesian approach.
2. Identify Least Informative Term: The explanatory term $h_i(\mathbf{x})$ whose corresponding coefficient θ_i exhibits the largest posterior Bayesian Coefficient of Variation (CoV) is identified. The CoV indicates the highest relative uncertainty, marking the term as the least informative contributor to the model.
3. Eliminate and Re-evaluate: The explanatory term identified as the least informative is excluded from the formulation, and the reduced model is re-calibrated to obtain updated posterior statistics. The simplification is deemed acceptable only if the posterior mean of the model error standard deviation, σ, does not exhibit a significant increase.

If the increase in σ is acceptable, the process repeats from Step 2. Otherwise, the elimination is rejected, and the model from the previous step is retained as the final, most parsimonious form. This iterative procedure ensures that only statistically insignificant terms are removed, preserving the model's predictive power.

3. Results and discussion

3.1. Quasi-static test results

The results of the quasi-static axial compression tests on CLT, CLBT1, and CLBT2 specimens including the stress–strain relationships, observed failure characteristics, and compressive strengths (derived from the stress–strain curves) provide the basis for selecting the stress levels applied in the subsequent long-term creep tests. In addition to characterizing the mechanical behaviour under short-term loading, a simplified bilinear constitutive model was developed to represent the compressive response of the CLBT1 and CLBT2 specimens.

3.1.1. Stress–strain relationships

Fig. 5 presents the stress–strain curves obtained from the quasi-static axial compression tests for the three materials (CLT, CLBT1, and CLBT2). For each material, five specimens were tested, and axial strain was measured using multiple strain gauges affixed to the specimen faces. The grey lines in the figure show individual stress–strain curves of each specimen, illustrating the inherent variability within each group.

To obtain a representative response for each material, an average stress–strain curve was constructed. Before averaging, each curve was truncated at peak stress to remove the post-peak softening segment, which can vary significantly between specimens. The remaining pre-peak segments were interpolated to a uniform strain range, and the mean stress was calculated at each corresponding strain value. The resulting average curve (solid black in Fig. 5) captures the typical compressive response of each material.

The average stress–strain curves shown in Fig. 5 reveal clear differences in the compressive behaviour of the three materials. To describe the observed mechanical behaviour in a simplified and consistent form, the constitutive model in Eq. (2), which captures both the initial elastic stiffness and the reduced tangent stiffness after yielding, was adopted for each material (as discussed in Section 2.2.1). A linear-elastic constitutive model (red line) was adopted for CLT, reflecting its near-linear response up to a brittle compressive failure; thus, nonlinear/post-peak effects were neglected in Eq. (2). In contrast, CLBT1 and CLBT2 exhibited a more progressive (ductile) response with a discernible post-yield stage; accordingly, a bilinear model (red and green lines) was used to capture both the initial elastic stiffness and the reduced tangent stiffness after yielding.

The compressive strength values listed in Table 2 were derived from the peak stresses recorded during the quasi-static compression tests, as illustrated in Fig. 5. Five tests were conducted for each material, yielding average compressive strengths (σ_{cu}) of 21.35 MPa for CLT, 22.82 MPa for CLBT1, and 29.18 MPa for CLBT2. The results indicate that both hybrid configurations exhibit higher compressive strength than the all-timber CLT, However, it should be noted that the specimens differ in their inner layer configurations and the net cross-sectional area of fibres loaded in the grain direction. Therefore, the observed increase in capacity reflects the structural performance of these specific hybrid layups rather than a direct material-level comparison. These average compressive strengths were subsequently used to define the stress levels for the long-term creep tests. Following previous research on compressive creep experiments of timber materials [75–77], the stress levels for the creep tests were established at 15% and 30% of the compressive strength for each material group, thereby ensuring that tertiary creep behaviour can be neglected. This resulted in target applied stresses of 3.20 MPa and 6.41 MPa for CLT, 3.42 MPa and 6.85 MPa for CLBT1, and 4.38 MPa and 8.75 MPa for CLBT2, as shown in Table 2.

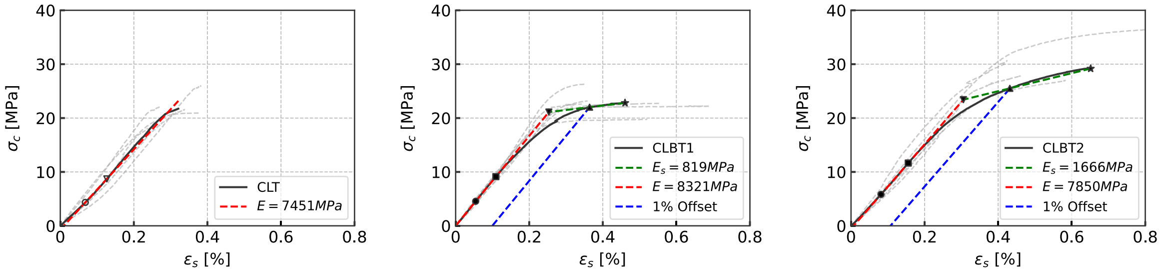

(a) (b) (c)

Fig. 5. Stress–strain curves obtained from quasi-static axial compression tests of the three specimen types. Each subfigure shows the individual stress–strain responses (grey lines) and the corresponding averaged curve (black line) for: (a) CLT, (b) CLBT1, and (c) CLBT2 specimens. The red and green dashed lines represent the initial elastic modulus E and secant modulus E_s. The blue dashed line is parallel to the initial elastic slope E, drawn from a strain of 0.1%. Hollow markers indicate the key characteristic points used for bilinear fitting: circle–corresponding to $0.2\sigma_{cu}$, inverted triangle–corresponding to $0.4\sigma_{cu}$, triangle–intersection with the 0.1% offset line, star–curve end (σ_{cu}), and square–intersection between lines.

Table 2
Compressive strength (σ_{cu}, MPa) of CLT, CLBT1, and CLBT2 specimens. The table presents individual test values, their mean, the coefficient of variation (COV), and the corresponding 30% and 15% compressive strength thresholds.

Specimen	No. 1	No. 2	No. 3	No. 4	No. 5	Mean	COV	30%	15%
CLT	21.59	20.96	18.06	22.17	25.98	21.35	0.136	6.41	3.20
CLBT1	23.19	19.77	22.25	22.62	26.29	22.82	0.100	6.85	3.42
CLBT2	27.00	27.83	22.11	38.25	30.72	29.18	0.206	8.75	4.38

3.1.2. Failure mode

Fig. 6 illustrates the typical deformation and failure progression observed during the quasi-static axial compression tests for CLT, CLBT1, and CLBT2 specimens. At the initial loading stage (Point A on the force–displacement curves), all specimens remained in the elastic regime. Strain distributions were relatively uniform across all types, with only minor localized concentrations near material heterogeneities. Surface features such as inter-laminar gaps and defects, especially in the transverse layers made of timber, were present before loading. These features were attributed to manufacturing-induced imperfections rather than early signs of mechanical damage. It is expected that these transverse layers exhibit more irregularities; however, due to their significantly lower stiffness perpendicular to the grain, they attract minimal load compared to the longitudinal layers and are therefore not the critical drivers of failure. The force–displacement curves during this phase exhibit a linear trend, confirming that the deformation was fully recoverable and no structural degradation had yet occurred.

At Point B, all specimens reached their peak load, marking the transition from stable deformation to the onset of material failure. Longitudinal cracks developed consistently in all specimen types and initiated along the inner faces of the outermost layers, often near the adhesive interfaces. Although imperfections existed in the central timber layer, the primary crack formation was concentrated at the bonding interfaces, likely due to localized interfacial stresses. These cracks, aligned with the axial loading direction, coincide with the peak of the force–displacement curve and mark the ultimate load-carrying capacity.

Between Points B and C is the post-peak phase, characterized by a drop in load with continued axial displacement. Earlier experimental studies on CLT under axial compression have shown that failure is typically governed by progressive crushing of the longitudinal layers and crack initiation along adhesive interfaces, rather than abrupt brittle fracture [78,79]. The compressive failure modes observed for the CLT and CLBT1 specimens in this study are generally consistent with those reported in previous literature. Crack propagation progressed along the bonding interfaces, and visible delamination was observed across all materials. Point C is the failure point: for CLT specimens, localized crushing near the loaded ends suggested compressive failure of the timber. Both CLBT1 and CLT maintained relatively stable descending branches in their force–displacement curves, with damage generally confined to localized zones. In contrast, the CLBT2 specimens exhibited a more brittle post-peak response. Extensive delamination occurred in the outer bamboo lamellae. Following this detachment, the loss of lateral restraint induced buckling of the outer layers, resulting in their outward separation from the core. This mechanism was accompanied by a more rapid reduction in load, indicating a less stable residual capacity

3.2. Creep tests results

3.2.1. Creep curves

The creep strain evolution over a 180-day period is shown in Fig. 7, where the subfigures (a), (c), (e) present the vertical creep strains of CLT, CLBT1, and CLBT2 specimens, (b), (d), (f) display the corresponding horizontal strains. The curves under 15% and 30% stress ratios exhibit comparable general trends across all specimen types, while also reflecting differences associated with material configuration.

For the vertical direction, three characteristic creep stages were identified. Immediately after load application, a short rebound in strain occurred, which can be attributed to self-equilibration of the loading system, seating effects, and redistribution of internal stresses. Following this transient adjustment, the primary stage (stage 1) featured a rapid increase in strain due to viscoelastic deformation and microstructural rearrangement under sustained load. As the tests progressed, the creep rate decreased, and the specimens gradually transitioned into the secondary stage (stage 2), characterized by a stabilized response. Because the applied stress ratios were relatively low, the tertiary stage of accelerated deformation was not observed. Across all materials, a relatively stable state was reached after approximately 60 days. By this time, the accumulated creep accounted for about 90%, 92%, and 86% of the total vertical creep strains (creep strains measured at 180 days) for CLT, CLBT1, and CLBT2, respectively. This finding underscores the dominant contribution of early-stage deformation to the overall long-term creep response.

In contrast, the horizontal creep curves displayed greater variability and fluctuations compared with the vertical ones. All three materials exhibited net lateral contraction over time, consistent with the Poisson effect, but the magnitude and stability varied by specimen type. The fluctuations are likely associated with the sensitivity of adhesive bond-lines and inter-laminar interfaces to hygrothermal changes in T and RH, which can temporarily alter stiffness and restraint, thereby influencing lateral strain development. Among the three materials, CLT exhibited the most pronounced fluctuations, suggesting greater hygrothermal sensitivity than CLBT1 and CLBT2.

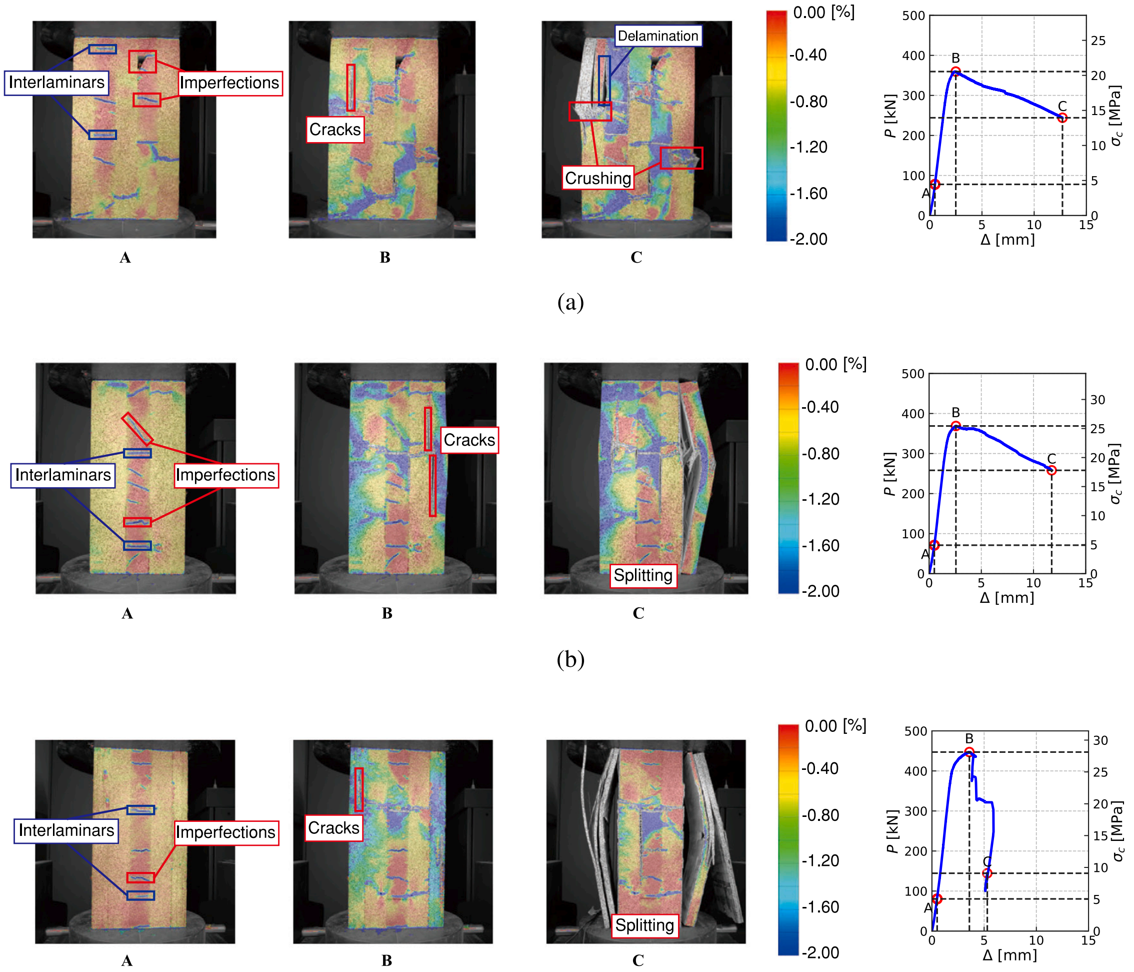

(a)

(b)

(c)

Fig. 6. Typical failure modes of (a) CLT, (b) CLBT1, and (c) CLBT2 specimens under axial compression. For each type, subfigures A–C show DIC images at different loading stages, and the corresponding points are marked on the load–displacement curves. The right-hand vertical axis indicates the corresponding compressive stress (σ_c), allowing direct comparison among specimens with different cross-sectional areas.

The results in Table 3 reveal distinct characteristics of vertical and horizontal creep under sustained compression. In the vertical direction, the elastic strains nearly doubled when the load increased from 15% to 30% of the ultimate capacity. These stress levels correspond to the initial linear portion of the stress–strain curves obtained from the quasi-static tests, suggesting that the material response remained primarily elastic. The maximum vertical creep strains increased with stress ratio, reaching 0.276%, 0.174%, and 0.269% for CLT, CLBT1, and CLBT2, respectively, under the 30% level, compared with 0.142%, 0.097%, and 0.184% at 15%. In contrast, the horizontal strains were consistently negative, reflecting a lateral contraction associated with Poisson's effect. The magnitude of horizontal creep increased with stress level, with CLT showing the largest lateral deformations (−0.450% at 30% stress), whereas CLBT1 and CLBT2 exhibited more moderate responses. Unlike the relatively smooth development of vertical strains, the horizontal creep curves displayed noticeable fluctuations throughout the loading period. Notably, the extremum values of horizontal strain correspond to the most negative readings, emphasizing that lateral contraction rather than expansion dominated the creep response. These findings highlight the anisotropic nature of the time-dependent deformation. Specifically, vertical creep was relatively stable and governed primarily by axial load level, while transverse creep (lateral contraction) exhibited greater fluctuations and higher sensitivity to hygrothermal variations and material configuration, particularly in CLT, where inter-laminar effects may have amplified lateral deformation.

To benchmark the test data against established findings, a comprehensive literature review was conducted. However, existing experimental studies on the creep behaviour of timber-like materials predominantly focus on bending and tension loading [80–82]; experimental data regarding compressive creep remains scarce. The available data are synthesized in Table 4. To ensure comparability across studies, the creep strain is along the fibre direction and represented by the dimensionless creep coefficient (ϕ_u), following the Eurocode methodology [83]. ϕ_u is calculated as the ratio of net creep strain (excluding the elastic strain) to elastic strain

$$\phi_u = \frac{\varepsilon_{vu} - \varepsilon_{ve}}{\varepsilon_{ve}}. \tag{11}$$

Literature values generally span $\phi_u \approx 0.48$–1.82 for timber-like columns under axial compression (varying in duration and load levels) [75–77]. Generally, the measured creep coefficients in this study fall within the range reported in the literature, while the present CLT ($\phi_u = 3.52$) and CLBT2 ($\phi_u = 2.52$) specimens at 15% moisture content slightly exceed this range. It must be noted that direct quantitative alignment is inherently difficult, as studies differ in test duration (120–360 days), stress ratio (10%–30%), material type, specimen geometry, and—critically—hygrothermal history. These factors

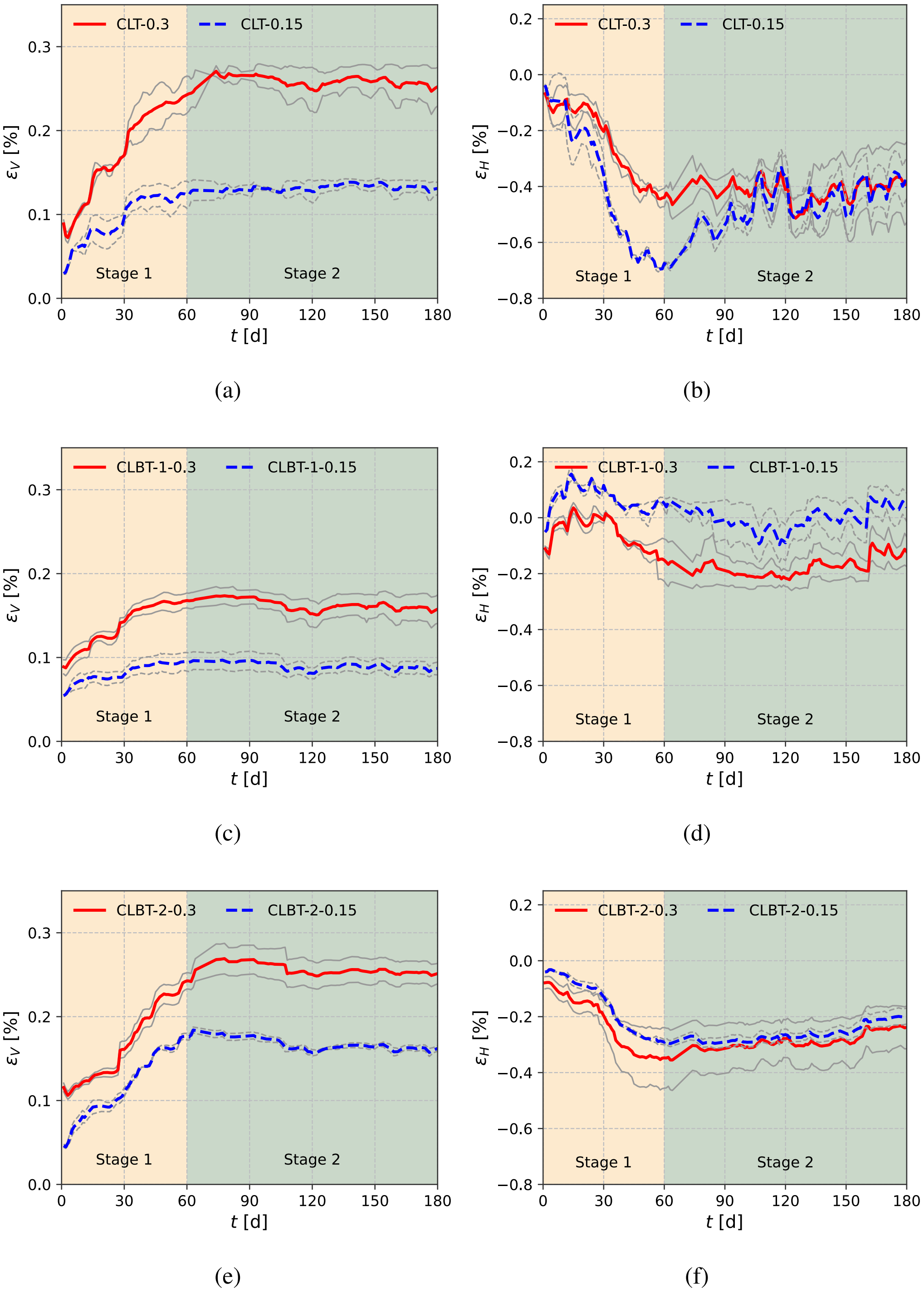

(a)
(b)
(c)
(d)
(e)
(f)

Fig. 7. Time-dependent creep curves of laminated bamboo-timber specimens. (a) vertical strain of CLT under stress ratios of 30% and 15%; (b) horizontal strain of CLT under stress ratios of 30% and 15%; (c) vertical strain of CLBT1 under stress ratios of 30% and 15%; (d) horizontal strain of CLBT1 under stress ratios of 30% and 15%; (e) vertical strain of CLBT2 under stress ratios of 30% and 15%; (f) horizontal strain of CLBT2 under stress ratios of 30% and 15%. The grey curves represent the two repeated tests, while the coloured curves denote the mean values. Here, ε_v represents vertical strain and ε_h represents horizontal strain.

significantly influence both ultimate creep strain (ε_{vu}) and the instantaneous elastic strain (ε_{ve}). As presented in Table 4, the CLBT1 material exhibited superior creep resistance compared to the other materials in this study, indicated by its relatively lower ϕ_u values (ranging from 0.61 to 0.79).

3.2.2. Hygrothermal data

The data collection started on November 15, 2024, and ended on May 15, 2025, spanning both the winter and spring seasons. Shown in Fig. 8, the blue curve represents real-time data collected every 15 min, reflecting the changes in Temperature (T) and Relative Humidity RH within the laboratory, which are influenced by the seasons, external climate, and indoor environment. Red lines are daily averages (mean of 96 readings/day), which smooth intraday fluctuations and highlight long-term trends.

Furthermore, from day 25 to day 70, and after day 160, the daily variation in the temperature curve was significant due to air-conditioning to regulate laboratory temperature during winter and

Table 3

The elastic strain and maximum creep strain were measured over 180 days for different specimens under various load levels. Here, F denotes the applied load. The strains were calculated based on the standard definition of strain as the ratio of deformation to the original gauge length. ε_{ve} and ε_{he} represent the instantaneous elastic strains in the vertical and horizontal directions, respectively, measured immediately after load application. ε_{vu} and ε_{hu} denote the corresponding maximum creep strains in the vertical and horizontal directions, obtained as the creep strain values at day 180. The symbols $\bar{\varepsilon}_{ve}$, $\bar{\varepsilon}_{he}$, $\bar{\varepsilon}_{vu}$ and $\bar{\varepsilon}_{hu}$ denote the mean values of ε_{ve}, ε_{he}, ε_{vu} and ε_{hu}, respectively, averaged over the same specimens tested under the same load level. As some creep strains in the horizontal direction are negative, the maximum value corresponds to the minimum (most negative) strain. All strain values are expressed as percentages, calculated as $(\Delta L/L_0) \times 100$.

Stress ratio	Type	F (kN)	ε_{ve} (%)	$\bar{\varepsilon}_{ve}$ (%)	ε_{vu} (%)	$\bar{\varepsilon}_{vu}$ (%)	ε_{he} (%)	$\bar{\varepsilon}_{he}$ (%)	ε_{hu} (%)	$\bar{\varepsilon}_{hu}$ (%)
0.3	CLT-1	104.0	0.084	0.089	0.231	0.254	−0.078	−0.069	−0.519	−0.376
	CLT-2	104.0	0.093		0.276		−0.058		−0.233	
	CLBT1-1	116.3	0.097	0.089	0.176	0.159	−0.102	−0.111	−0.180	−0.131
	CLBT1-2	116.3	0.080		0.142		−0.120		−0.082	
	CLBT2-1	135.2	0.121	0.115	0.264	0.252	−0.057	−0.078	−0.159	−0.237
	CLBT2-2	135.2	0.110		0.240		−0.100		−0.314	
0.15	CLT-1	53.2	0.030	0.029	0.138	0.131	−0.033	−0.038	−0.443	−0.369
	CLT-2	53.2	0.029		0.124		−0.042		−0.295	
	CLBT1-1	58.1	0.053	0.054	0.079	0.087	−0.052	−0.051	0.088	0.037
	CLBT1-2	58.1	0.056		0.095		−0.050		−0.014	
	CLBT2-1	68.3	0.048	0.046	0.159	0.162	−0.043	−0.040	−0.227	−0.198
	CLBT2-2	68.3	0.044		0.165		−0.038		−0.170	

Table 4

Comparison of creep behaviour along the fibre direction with literature for engineered wood columns under axial compression. The load level is expressed as a percentage of the compressive strength (σ_{cu}) measured from quasi-static tests. The elastic strain (ε_{ve}) represents the instantaneous strain measured immediately after loading. The ultimate creep strain (ε_{vu}) represents the creep strain (sum of the elastic strain and net creep strain) at the last day of the test (e.g., the creep strain at 180 days in this study). All strain values are given as percentages.

Reference	Material type	Load level (%)	σ_{cu} (MPa)	Duration (days)	ε_{ve} (%)	ε_{vu} (%)	ϕ_u
Present study	CLT	15	21.35	180	0.029	0.131	3.52
	CLT	30			0.089	0.254	1.85
	CLBT1	15	22.82		0.054	0.087	0.61
	CLBT1	30			0.089	0.159	0.79
	CLBT2	15	29.18		0.046	0.162	2.52
	CLBT2	30			0.115	0.252	1.19
Sun et al. [75]	CLT	10	18.65	330	–	–	1.49
	CLT	20					1.82
Zheng et al. [76]	Wood	20	47.73	360	–	–	0.747
Nguyen et al. [77]	CLT	10	24.1	120	0.040	0.059	0.48

summer. This led to larger temperature fluctuations (increased amplitude). The RH curve is also influenced by temperature changes. Frequent fluctuations in temperature may lead to fluctuations in humidity, especially when the air conditioning is running, making the relationship between temperature and humidity more sensitive.

To quantify the influence of environmental factors on long-term deformation, a correlation analysis was performed between the measured vertical creep strains and the recorded temperature (T) and absolute humidity (AH) histories. The analysis employed a simple linear regression model of the form $\varepsilon = aX + b$, where ε denotes the normalized creep strain and X represents the environmental variable (T or AH). The parameters a and b correspond to the slope and intercept of the fitted line, respectively, reflecting the sensitivity and baseline level of creep strain with respect to each environmental factor. For consistency, the regression was conducted using the creep strain values measured after 60 days, representing the stabilized stage of time-dependent deformation.

The fitted regression results are illustrated in Fig. 9, while the corresponding parameters for all specimen types and stress levels are summarized in Table A.1. As noted in numerous studies [84–86], variations in environmental temperature and humidity significantly influence creep deformation. Regarding temperature, the analysis reveals a general trend where compressive creep strain decreases as T increases. The average slope and intercept across all specimen types and stress levels were $\bar{a} = -1.39 \times 10^{-3}$ (COV = 57.9%) and $\bar{b} = 0.19$ (COV = 37.00%), respectively. The influence of Absolute Humidity (AH) on compressive creep strain generally exhibited a negative correlation, although this effect appeared less pronounced in specimens subjected to higher stress levels. The corresponding mean values were $\bar{a} = -6.64 \times 10^{-4}$ (COV = 169.00%) and $\bar{b} = 0.17$ (COV = 29.40%). Notably, for both temperature and humidity, the creep response under higher stress levels exhibited larger variance, as indicated by the wider prediction bands (blue dashed lines) in the figures.

Physically, the impact of ambient temperature and humidity on the long-term creep of fibrous matrices is primarily attributed to the mechano-sorptive effect, resulting from fluctuations in internal moisture content [20,80,86,87]. In the specific context of compressive creep in timber-based materials, moisture adsorption is known to accelerate creep recovery (reducing apparent compressive strain) [85]; this mechanism is consistent with the experimental observations of this study. Concurrently, thermal fluctuations modulate material stiffness, thereby altering creep response [88]. It is also notable that residual hygrothermal effects introduce unavoidable variations in the creep data, as the non-stressed control specimens cannot perfectly replicate the complex internal moisture gradients of the loaded specimens. Given that the coupled influence of temperature and humidity on fibrous materials is intricate and lacks a universally accepted deterministic physical model [85,86], the following section proposes a physically based phenomenological probabilistic model. This framework aims to rigorously quantify these complex environmental effects and their inherent uncertainties.

4. Calibration of the predictive models

4.1. Deterministic model

The fitting was applied jointly to the datasets at 15% and 30% load levels, thus yielding a single parameter set for each material type. To

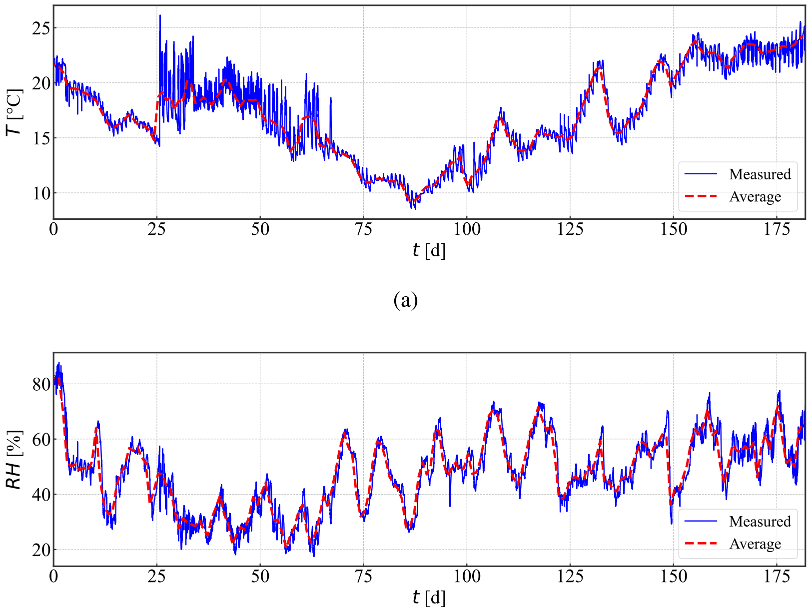

(a)

(b)

Fig. 8. (a) Temperature and (b) relative humidity in hygrothermal information during the creep tests. T represents the temperature and RH represents the relative humidity.

Table 5

Calibrated Burgers parameters and fit metrics (units: E in MPa, η in MPa d).

Material	E_e	E_d	η_d	η_v	R^2	MAE	RMSE
CLT	9854.71	2952.10	7.88×10^4	1.00×10^9	0.855	3.02×10^{-2}	3.54×10^{-2}
CLBT1	8420.80	10 494.48	1.83×10^5	1.00×10^9	0.435	1.94×10^{-2}	2.43×10^{-2}
CLBT2	11 454.66	3809.77	1.12×10^5	1.00×10^9	0.662	4.26×10^{-2}	4.88×10^{-2}

evaluate the quality of fit, three statistical indicators were computed: the coefficient of determination (R^2), the mean absolute error (MAE), and the Root Mean Square Error (RMSE). Representative comparisons between measured and predicted compliance curves, together with predicted-versus-measured scatter plots, are presented in Fig. 10. The calibrated parameter values for CLT, CLBT1, and CLBT2, along with the associated error metrics, are summarized in Table 5.

As summarized in Table 5, the calibrated Burgers parameters exhibit physically consistent trends among the three materials. The instantaneous modulus E_e is close to, though slightly higher than, the elastic modulus obtained from the static compression tests, reflecting the idealized assumption of purely elastic behaviour during the initial loading stage. Both the delayed modulus E_d and the retarded viscosity η_d of the CLBT specimens are higher than those of CLT, with CLBT1 showing the maximum values (E_d = 10.49 GPa, $\eta_\mathrm{d} = 1.83 \times 10^5$ MPa d). In the Burgers formulation, E_d represents the stiffness of the Kelvin–Voigt element and thus governs the magnitude of the retarded elastic deformation, while η_d controls its rate of development through the time constant $\tau_d = \eta_\mathrm{d}/E_\mathrm{d}$. The higher E_d and η_d values of the CLBT specimens, particularly CLBT1, indicate that the bamboo layers enhance the resistance to time-dependent deformation and slow down viscoelastic relaxation during the transient creep stage. In contrast, the permanent viscosity η_v reaches its upper bound (1.0×10^9 MPa d) for all specimens, implying negligible contribution from the viscous flow term $(\sigma_0/\eta_\mathrm{v})t$ within the 180-day test duration. While these calibrated parameters capture the general viscoelastic behaviour, the overestimated elastic moduli and material-dependent variations highlight the limitations of deterministic calibration. To better represent such uncertainties and capture the intrinsic variability of the creep process, a probabilistic correction model is developed in the following section.

Fig. 10 compares the measured creep compliance with the Burgers model predictions for CLT, CLBT1, and CLBT2. The calibrated model reproduced the overall time-dependent compliance trends, with the best agreement obtained for CLT (R^2 = 0.855, MAE = 0.030, RMSE = 0.035). For CLBT2, the fit was moderate (R^2 = 0.662, MAE = 0.043, RMSE = 0.049), while CLBT1 exhibited the lowest accuracy (R^2 = 0.435, MAE = 0.019, RMSE = 0.024). These results indicate that, although the Burgers model captures the general creep response of all three materials, its predictive accuracy varies with material type. The variability in fitting accuracy, most notably the comparatively low R^2 values for CLBT1 and CLBT2, underscores the role of intrinsic material heterogeneity and experimental scatter in the observed creep response. While the Burgers model offers a mechanistic backbone for viscoelastic deformation, the dispersion of the fitted responses indicates that a purely deterministic calibration cannot capture the full behavioural spectrum. To address this limitation, the next section introduces a probabilistic modelling framework.

4.2. Probabilistic models

The probabilistic modelling framework (*i*) treats key parameters as random variables to reflect epistemic and aleatory uncertainties and (*ii*) augments the mean response with additional explanatory functions of the hygrothermal state to encode climate sensitivity. Specifically, T and AH will be added as parsimonious co-variates, enabling environment-conditioned creep predictions and quantitative reliability metrics for long-term performance.

The set of candidate explanatory functions $\mathbf{h}(\mathbf{x}) = [h_1(\mathbf{x}), h_2(\mathbf{x}), \ldots, h_p(\mathbf{x})]$ for the correction term (Eq. (9)) is summarized in Table 6. These functions are derived from the hygrothermal variables temperature (T) and absolute humidity (AH), and transformed into standardized, dimensionless forms $S[\cdot]$ according to Eq. (10). The instantaneous effects of hygrothermal fluctuations are represented by $S[T]$ and $S[AH]$,

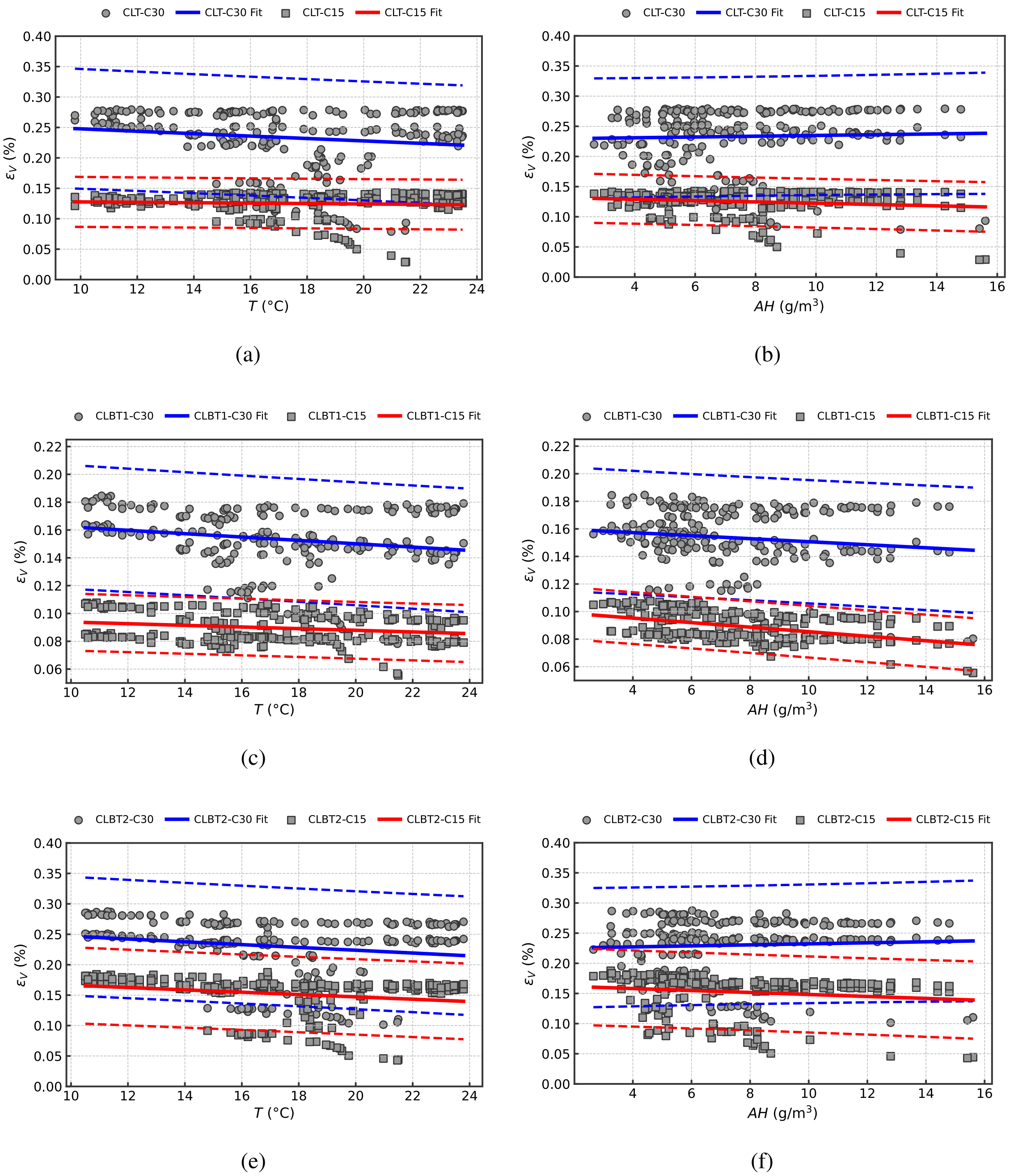

(a) (b)

(c) (d)

(e) (f)

Fig. 9. Correlation analysis of creep strain after 60 days with temperature T (a,c,e) and absolute humidity AH (b,d,f) for CLT, CLBT1, and CLBT2, respectively. Solid lines denote linear regression fits, and dashed lines indicate the 95% prediction bands.

together with their squared terms $S[T^2]$ and $S[AH^2]$. To account for long-term exposure, the cumulative sums $\sum S[T]$ and $\sum S[AH]$ are introduced, while the cumulative squared terms $\sum S[T^2]$ and $\sum S[AH^2]$ capture potential nonlinear history effects. For each function, descriptive statistics (maximum, minimum, mean, and standard deviation) are reported to characterize their variability. These functions form the candidate pool for the stepwise selection procedure used to identify the most suitable explanatory form of the correction term in the probabilistic model.

Fig. 11 shows the results of the stepwise deletion procedure applied to refine the probabilistic creep compliance models. For example, in the first step of the CLBT1 model, θ_8 was removed due to its large posterior coefficient of variation, indicating a weak contribution to explaining the variability of the data. The procedure then continued by successively discarding other low-information terms, while monitoring the posterior mean of the model error standard deviation σ. Elimination was accepted only if the resulting increase in the posterior mean of the model standard deviation σ remained negligible, ensuring a conservative balance between model parsimony and predictive accuracy. The procedure terminated once further removal would have produced a non-negligible increase in σ, indicating loss of explanatory power for subtle hygrothermal influences. As a result, the final reduced models for CLT, CLBT1 and CLBT2 retained only a small subset of explanatory functions (Tables B.3–B.4), while preserving predictive performance comparable to the full models.

Tables B.3–B.4 present the posterior statistics of the selected probabilistic creep models and their pairwise correlations. The stepwise elimination process identified different explanatory functions for each material system. For CLT, the final model retained $h_2 = S[AH]$ and $h_5 = S[T^2]$, corresponding to the standardized instantaneous effects of

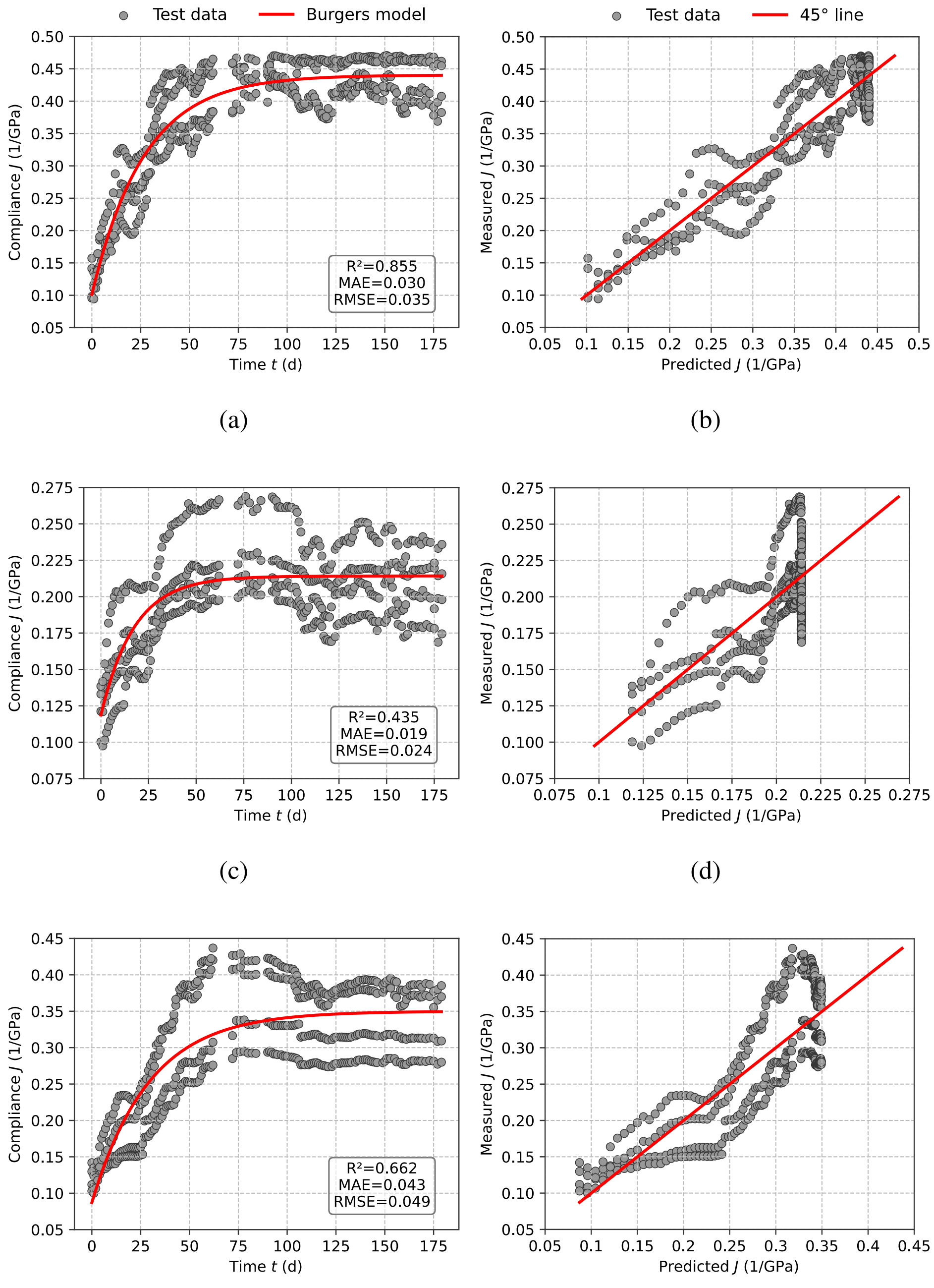

(a) (b)

(c) (d)

(e) (f)

Fig. 10. Comparison between experimental data and Burgers model predictions for the three materials. The subfigures (a) and (b) correspond to CLT specimens, (c) and (d) to CLBT1, and (e) and (f) to CLBT2. In each left-hand plot, the creep compliance $J(t)$ is shown against time, while the corresponding right-hand plot compares predicted versus measured values.

Table 6
Candidate explanatory functions for $\gamma(\mathbf{x}, \boldsymbol{\Theta}_c)$. Reported are the maximum, minimum, mean, and standard deviation (SD) of each standardized variable.

ID	Variables	Max	Min	Mean	SD	ID	Variables	Max	Min	Mean	SD
$h_1(\mathbf{x})$	$S[T]$	1.7604	−2.1967	6.52×10^{-16}	1	$h_5(\mathbf{x})$	$S[T^2]$	1.9885	−1.8268	3.31×10^{-17}	1
$h_2(\mathbf{x})$	$S[AH]$	2.9970	−1.6474	-9.76×10^{-17}	1	$h_6(\mathbf{x})$	$S[AH^2]$	3.8067	−1.1066	1.10×10^{-16}	1
$h_3(\mathbf{x})$	$\sum S[T]$	12.4464	−38.9215	−9.8196	18.0378	$h_7(\mathbf{x})$	$\sum S[T^2]$	8.8745	−41.1070	−11.985	17.9677
$h_4(\mathbf{x})$	$\sum S[AH]$	11.5251	−37.3145	−16.2155	17.4063	$h_8(\mathbf{x})$	$\sum S[AH^2]$	11.7047	−34.6962	−15.0144	16.3594

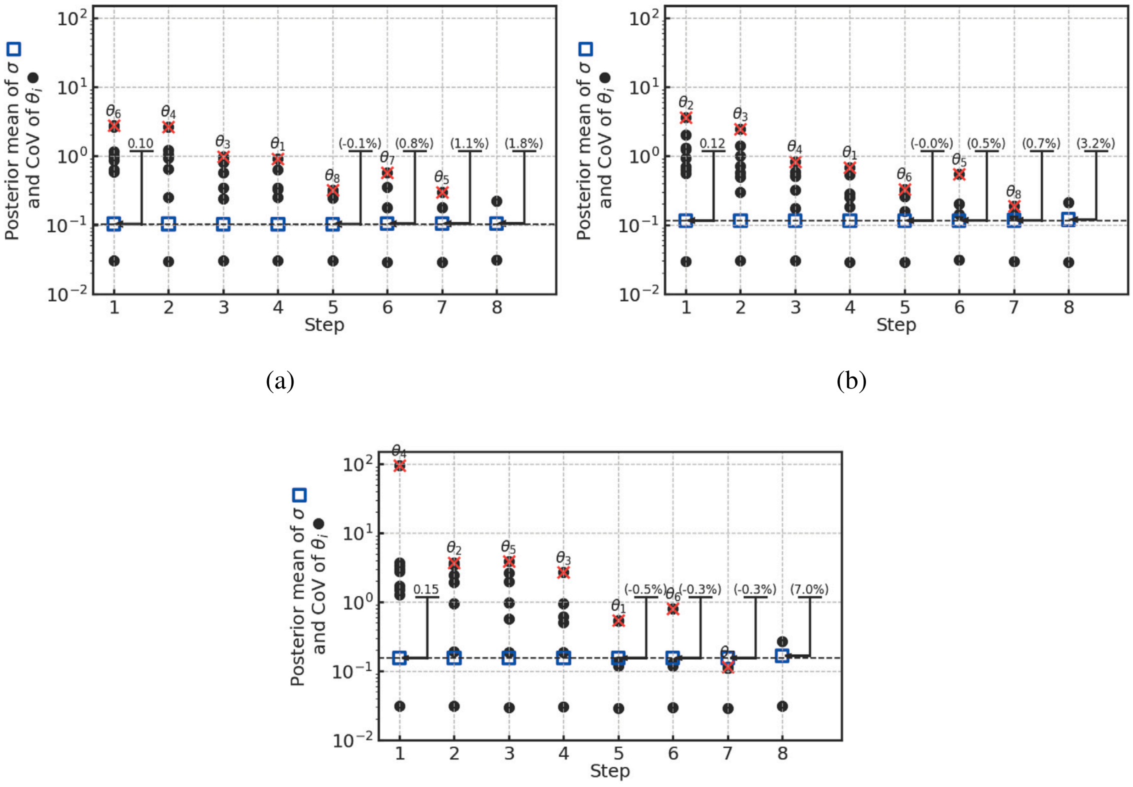

(a)

(b)

(c)

Fig. 11. Stepwise deletion process for the probabilistic creep compliance models of laminated bamboo–timber composites: (a) CLT, (b) CLBT1, and (c) CLBT2. Each step shows the posterior mean of the model standard deviation σ (squares) and the coefficients of variation (CoV) of the retained parameters θ_i (dots). Dots marked with a cross indicate parameters removed in that step. The dashed black line denotes the initial value of σ, used as a reference across iterations. Annotated values of σ at the final steps highlight the cumulative change during the reduction process.

humidity and temperature fluctuations. In contrast, both CLBT1 and CLBT2 adopted $h_7 = \sum S[T^2]$ and $h_8 = \sum S[AH^2]$, which represent the cumulative squared variations of temperature and humidity, respectively. The selection of these functions indicates that the creep behaviour of the laminated bamboo–timber composites is more sensitive to the long-term accumulation of hygrothermal exposure, whereas the all-timber CLT is primarily governed by short-term fluctuations.

As shown in Tables B.3–B.4, the posterior distributions of the Burgers model parameters (E_e, E_d, η_d, η_v) obtained from the probabilistic fitting exhibit narrower uncertainty bounds and more physically consistent mean values compared with those calibrated from the deterministic regression. In particular, the mean values of E_e are closer to the elastic moduli measured in the static compression tests, confirming that the probabilistic model provides a more realistic representation of the instantaneous elastic response. The other parameters follow similar trends to those observed in the deterministic analysis, with E_d and η_d of the CLBT specimens remaining higher than those of CLT, reflecting the influence of bamboo layers on transient viscoelastic resistance. Overall, the probabilistic calibration not only accounts for model uncertainty and environmental variability but also refines the Burgers parameters towards values that are more consistent with the material's physical behaviour. In general, the probabilistic model enhances the explanatory capability of the Burgers formulation for the creep behaviour of all three materials, providing a more comprehensive and physically grounded interpretation of their time-dependent deformation.

For the probabilistic extensions of the Burgers model, different hygrothermal correction terms were retained for each material. With $\varepsilon_{\mathrm{N}} \sim \mathcal{N}(0,1)$, the three models read

$$J_{\mathrm{CLT}} = [\frac{1}{E_{\mathrm{e}}} + \frac{1}{E_{\mathrm{d}}}\left(1 - e^{-\frac{E_{\mathrm{d}}}{\eta_{\mathrm{d}}}t}\right) + \frac{t}{\eta_{\mathrm{v}}}] \cdot e^{\theta_2\left[\frac{T(t)-17.36}{3.47}\right]^2 + \theta_5\left[\frac{AH(t)-7.24}{2.80}\right]^2 + \sigma\,\varepsilon_{\mathrm{N}}} \tag{12}$$

$$J_{\mathrm{CLBT1}} = [\frac{1}{E_{\mathrm{e}}} + \frac{1}{E_{\mathrm{d}}}\left(1 - e^{-\frac{E_{\mathrm{d}}}{\eta_{\mathrm{d}}}t}\right) + \frac{t}{\eta_{\mathrm{v}}}] \cdot e_7^{\theta} \sum_{k=0}^{t}[\frac{T^2(k)-313.50}{119.99}] + \theta_8 \sum_{k=0}^{t}[\frac{AH^2(k)-60.20}{48.43}] + \sigma\,\varepsilon_{\mathrm{N}}\ , \tag{13}$$

$$J_{\mathrm{CLBT2}} = [\frac{1}{E_{\mathrm{e}}} + \frac{1}{E_{\mathrm{d}}}\left(1 - e^{-\frac{E_{\mathrm{d}}}{\eta_{\mathrm{d}}}t}\right) + \frac{t}{\eta_{\mathrm{v}}}] \cdot e_7^{\theta} \sum_{k=0}^{t}[\frac{T^2(k)-313.50}{119.99}] + \theta_8 \sum_{k=0}^{t}[\frac{AH^2(k)-60.20}{48.43}] + \sigma\,\varepsilon_{\mathrm{N}}\ . \tag{14}$$

Fig. 12 presents the prediction performance of the probabilistic models after the stepwise correction process, while Fig. 10 shows the baseline predictions of the deterministic Burgers model for reference. The deterministic Burgers model captured the general trend of creep compliance but exhibited clear differences in predictive accuracy, with CLT showing the best agreement (R^2 = 0.859, MAE = 0.030, RMSE = 0.035), followed by CLBT2 (R^2 = 0.706, MAE = 0.041, RMSE = 0.046), and CLBT1 the lowest (R^2 = 0.485, MAE = 0.019, RMSE = 0.023). Part of the relatively low R^2 values can be attributed to measurement uncertainties and the inherent variability of bio-based materials, which introduce scatter in the experimental data. Importantly, the probabilistic models incorporating correction terms consistently improved the R^2 compared with the uncorrected Burgers model, demonstrating their ability to account for stochastic effects. A noteworthy observation is that the explanatory functions selected for CLBT1 and CLBT2 share common terms (h_7 and h_8), suggesting that their creep response is influenced by similar mechanisms, likely associated with the bamboo layers

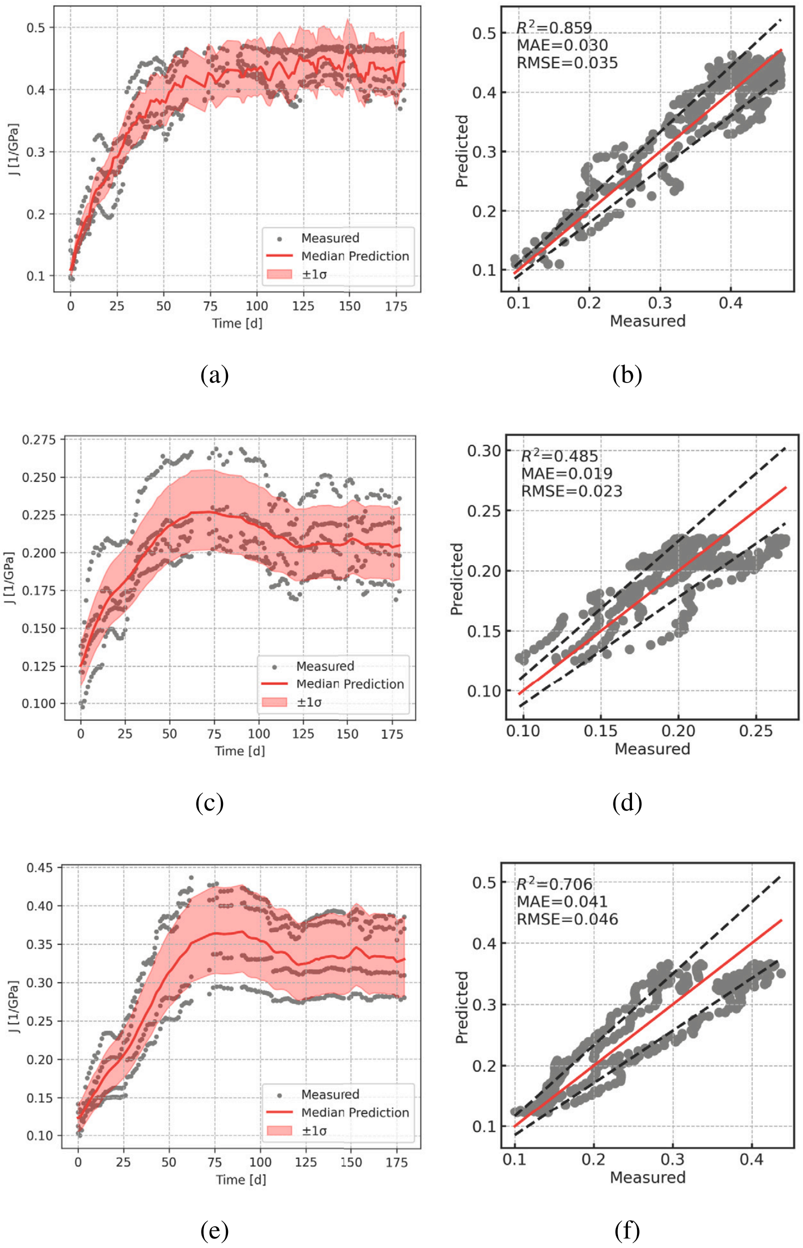

Fig. 12. Predictions generated by the proposed model: (a) predicted creep curves of CLT, (b) predicted value vs. measured value of CLT. (c) predicted creep curves of CLBT1, (d) predicted value vs. measured value of CLBT1. (e) predicted creep curves of CLBT2, (f) predicted value vs. measured value of CLBT2.

that are more sensitive to moisture fluctuations and micro structural heterogeneity. In contrast, the CLT model retained h_2 and h_5, reflecting a different sensitivity pattern that corresponds to the relatively uniform timber lamellae and their more stable hygro-mechanical behaviour. The larger variance observed in the cross-laminated bamboo-timber (CLBT1 and CLBT2) compared with CLT thus appears closely related to the introduction of bamboo layers, which, while enhancing strength, also increase variability in long-term creep response. Overall, these comparisons indicate that while the deterministic Burgers model provides a useful baseline, the probabilistic framework captures both the viscoelastic baseline behaviour and the variability arising from hygrothermal and material heterogeneities, thereby enhancing predictive robustness.

5. Example of application

The probabilistic creep models developed in this study (Section 4.2) are embedded in a finite element (FE) workflow built in OpenSeesPy [89] to quantify how long-term column deformation redistributes bending demand in a simple frame. It is emphasized that this numerical example is primarily demonstrative, intended to illustrate the reliability-based assessment workflow. Consequently, time-dependent deformation is restricted to the column element, while the extension to beam bending creep is reserved for future investigation, as it requires dedicated flexural calibration data distinct from the available uniaxial results. The example considers a CLBT1 beam supported at mid-span by a CLBT1 column. Creep acts only in the column; the beam responds elastically with geometric nonlinearity (the P–Δ effect). The goal is to propagate component-level viscoelasticity, conditioned on recorded climate, to the system scale for serviceability and reliability assessment.

5.1. FE model setup

The frame is two-dimensional and composed of: (i) a prismatic CLBT1 beam of span $L_b = 7.0$ m with rectangular section $b \times h =$

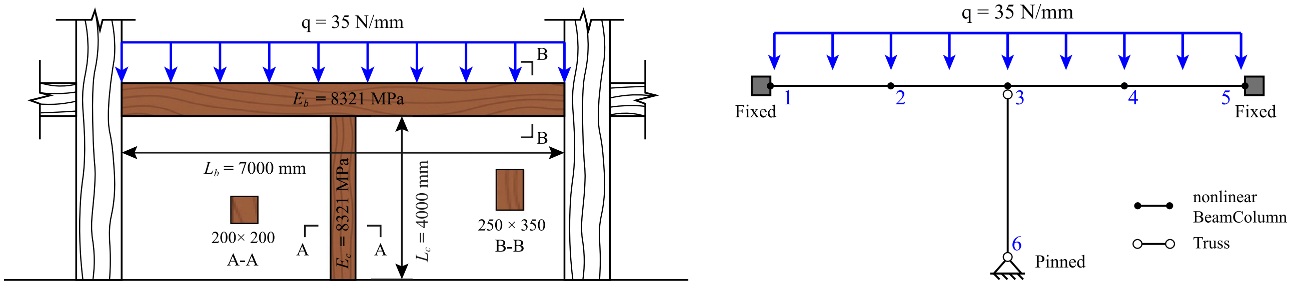

(a) (b)

Fig. 13. Representative frame with a mid-span CLBT support column. (a) geometry and loading; (b) OpenSeesPy model.

0.25×0.35 m^2; and (ii) a central CLBT1 column of height $L_c = 4.0$ m with square section 0.20×0.20 m^2 (Fig. 13). The material parameters and hygrothermal conditions were defined to match those experimentally characterized for the CLBT1 specimens, with the elastic modulus ($E_b = E_c = 8321$ MPa) adopted from the quasi-static compression tests (Section 3.1) and the time-varying temperature-humidity profiles taken from the recorded hygrothermal data in creep tests (Section 3.2.2). The beam is discretized into four `nonlinearBeamColumn` elements; section response is integrated with five-point Lobatto quadrature and geometric nonlinearity is accounted for via a `PDelta` transformation. The column is modelled as a `truss` element that transfers only axial force. The beam ends are fixed, while the column base is pinned; the column top is rigidly connected to the beam by sharing the mid-span node. A uniformly distributed line load $w = 35$ N/mm (downward) is applied to all beam elements using the `eleLoad -beamUniform` command.

Creep in the column is imposed by embedding an elastic uniaxial material within the `InitStrainMaterial` wrapper and prescribing a day-dependent initial strain. The analysis proceeds in daily increments over the available climate record (180 days in the provided dataset). For each day, the workflow is as follows:

1. Baseline static step: Perform a load-controlled static analysis under w to obtain the axial stress in the column, denoted as σ_{col}, representing the service stress. This step already accounts for the instantaneous elastic strain.
2. Creep prediction: Compute the time-dependent creep compliance of the column using the calibrated temperature–humidity-dependent model, and remove the instantaneous elastic component by evaluating the incremental compliance from $t = 0$ (defined as the instant immediately after load application), such that only the time-dependent (viscoelastic) deformation is retained.
$$\Delta J(t) = J(t) - J(t=0), \tag{15}$$
where $J(t)$ is given by the full Burgers form including the hygrothermal scaling (as shown in Eq. (13)), with the parameters taken from Table B.2.
The hygrothermal factor is constructed from the cumulative sums of daily mean temperature T and AH measured in the experimental tests (see Fig. 8, RH converted to AH via Eq. (6)). The day-t viscoelastic creep strain is then obtained as
$$\varepsilon_c(t) = \Delta J(t)\,\sigma_{\mathrm{col}}. \tag{16}$$
3. Reanalysis with imposed strain: Assign $\varepsilon_c(t)$ to the `InitStrainMaterial` of the column (truss) and rerun the static analysis to update the beam's bending-moment distribution.

This procedure yields, for each day t, the bending-moment diagram along the beam and the corresponding maximum bending moment $M_{\max}(t)$.

5.2. Inclusion of uncertainties

Aleatory uncertainty enters through the probabilistic creep model as an error term $\varepsilon_{\mathrm{N}} \sim \mathcal{N}(0,1)$ multiplying the hygrothermal correction. Uncertainty is propagated by explicit Monte Carlo simulation with $M = 500$ realizations: for each sample of ε_{N} and for each day t, the creep strain $\varepsilon_c(t, \varepsilon_{\mathrm{N}})$ is computed and a full FE reanalysis is carried out to obtain $M_{\max}(t, \varepsilon_{\mathrm{N}})$. This produces an ensemble of daily moment trajectories $\{M_{\max}(t, \varepsilon_{N,k})\}_{k=1}^{M}$, from which point-wise statistics and confidence bands are extracted.

The bending resistance of the beam was evaluated under elastic assumptions as

$$M_{\mathrm{cap}} = \sigma_{\mathrm{b}} \frac{b\,h^2}{6}, \tag{17}$$

where σ_{b} denotes the bending strength of the CLBT2 material. In accordance with the reliability analysis implemented in the script, σ_{b} is treated as a lognormally distributed random variable with a mean value of $\mu_{\sigma_b} = 25$ MPa and a coefficient of variation $\mathrm{CoV}_{\sigma_b} = 0.25$. The adopted variability is consistent with the recommendations of the JCSS Probabilistic Model Code [65], which provides reference values for the bending strength of structural timber.

The daily survival probability of the component is then computed as

$$P_{\mathrm{surv}}(t) = \mathbb{P}\big[M_{\mathrm{cap}} > M_{\max}(t, \varepsilon_{\mathrm{N}})\big], \tag{18}$$

where failure is defined by the limit state $g(t, \mathbf{X}) = M_{\mathrm{cap}}(\mathbf{X}) - M_{\max}(t, \mathbf{X}) \le 0$.

This probability is evaluated with the First-Order Reliability Method (FORM): the basic random variables $\mathbf{X}$ (e.g., tensile strength, creep-model error) are transformed to an uncorrelated standard normal space $\mathbf{U}$; the most probable failure point (design point) $\mathbf{u}^*$ on $g = 0$ is found by an iterative, gradient-based search; the reliability index is $\beta(t) = \|\mathbf{u}^*\|$; and the daily failure probability is approximated as $P_{\mathrm{f}}(t) \approx \Phi\big(-\beta(t)\big)$, with $\Phi(\cdot)$ the standard normal Cumulative Distribution Function (CDF). Hence, $P_{\mathrm{surv}}(t) = 1 - P_{\mathrm{f}}(t)$.

5.3. Results

Fig. 14 compares the bending-moment distribution at load application ($t = 0$) with that obtained at the end of the climate record ($t = 179$). As the column creeps and shortens, mid-span moments decrease while end moments grow modestly, evidencing a progressive shift of bending demand towards the fixed supports. The redistribution trend is monotonic and becomes less pronounced as $J(t)$ approaches its asymptote.

The time history of $M_{\max}(t)$ exhibits a gradual reduction over the first months, with a decreasing rate as the Kelvin branch saturates (Fig. 15). The Monte Carlo realizations (500 samples) quantify the dispersion due to the stochastic correction in the creep law: despite visible spread, all trajectories share the same qualitative trend and converge towards

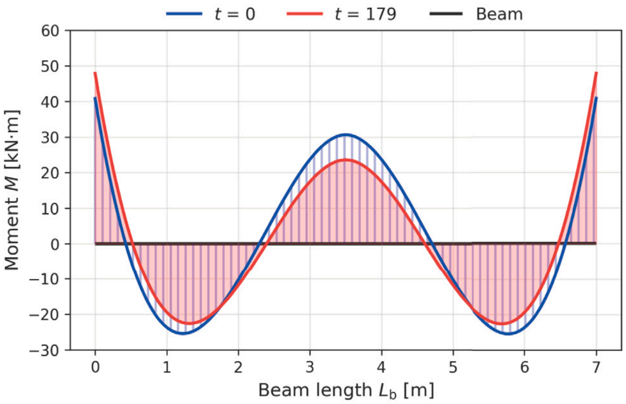

Fig. 14. Bending-moment distribution along the beam length ($M(L_b)$) at $t = 0$ and at the final day of the climate sequence ($t = 179$).

a stable band. The survival-probability curve, the complement of the fragility, starts near unity, decreases as creep demand grows relative to resistance, and stabilizes once the viscoelastic contribution becomes quasi-stationary.

The results indicate an initial survival probability very close to unity, which gradually decreases as creep strain accumulates and the applied demand approaches the probabilistic resistance. Specifically, the initial survival probability was approximately $P_{\mathrm{surv}} = 0.998$, corresponding to a reliability index of $\beta = 2.94$. By around $t = 77$ days, it had decreased to $P_{\mathrm{surv}} = 0.982$ ($\beta = 2.11$), representing a reduction of about 28.3% in the reliability index. This probabilistic assessment highlights the impact of long-term creep deformation on the system reliability, quantifying both the time-dependent reduction in safety margin and the eventual stabilization of failure probability.

The example shows how climate-aware, probabilistic creep at the component level can be embedded in routine OpenSeesPy analyses to obtain decision-grade, time-dependent demand and reliability metrics for CLBT systems.

6. Conclusions

This research combines experiments and modelling to characterize the compressive creep behaviour of three panels made of different materials: conventional CLT, CLBT with thick-strip GluBam (CLBT1), and CLBT with thin-strip GluBam (CLBT2). Short-term compression tests established baseline stiffness and strength, while 180-day sustained-load tests under recorded temperature and AH isolated time-dependent deformation with the aid of unloaded controls. A probabilistic compliance model with a Burgers backbone and hygrothermal co-variates was calibrated and embedded in OpenSeesPy to propagate component-level creep to system-level demand and reliability. Key findings are:

1. CLT exhibited an essentially linear elastic response up to failure, whereas CLBT1 and CLBT2 showed bilinear trends with post-yield stiffness reduction, indicating enhanced ductility of the bamboo–timber laminates in monotonic compression. In the quasi-static tests, the three material configurations exhibited distinct mean compressive strengths: 21.35 MPa for CLT, 22.82 MPa for CLBT1, and 29.18 MPa for CLBT2. It is important to note that these values represent the system-level performance of the specific heterogeneous layups rather than a direct material reinforcement effect, as the internal layer geometries differed between groups; nonetheless, the results indicate that the hybrid CLBT2 configuration achieved the highest load-bearing efficiency among the tested variants.
2. The vertical creep response for both CLT and CLBT specimens exhibited a stable, two-stage deformation pattern (primary and secondary) without entering the tertiary failure stage. In the loading direction, the ultimate creep strain was comparable to values reported in existing literature; notably, approximately 90% of the total 180-day strain was accumulated within the first 60 days. The horizontal creep strain exhibited heightened sensitivity to environmental fluctuations, a phenomenon potentially attributable to hygrothermal effects on the adhesive bond lines. Compared to CLT, the bamboo-timber composites (CLBT1 and CLBT2) demonstrated superior creep resistance, evidenced by lower ultimate creep coefficients in the loading direction and relatively more stable horizontal creep strain.
3. Temperature and humidity significantly influence the long-term creep behaviour; however, due to the complex physical coupling between these variables, their combined effect is not yet fully described by a universally accepted physical model.
4. Deterministic Burgers fits captured the average compliance trends but left non-negligible dispersion, especially for CLBT1 and CLBT2. The probabilistic framework, augmented with parsimonious hygrothermal functions, quantified parameter uncertainty and model error, enabling environment-conditioned predictions with confidence intervals suitable for performance-based design checks and the calibration of partial safety factors.
5. The posterior means of the Burgers parameters derived from the probabilistic calibration exhibited narrower uncertainty bounds and more physically consistent values than their deterministic counterparts. In particular, E_e closely matched the elastic moduli obtained from static compression tests, demonstrating that the probabilistic formulation enhances both the interpretability and predictive reliability of the Burgers model across all material systems.
6. The parameters E_d and η_d of the CLBT specimens were higher than those of CLT, especially for CLBT1, indicating that the inclusion of bamboo layers enhances the material's resistance to creep by suppressing the retarded viscoelastic deformation component-reducing both the magnitude and rate of delayed strain development. Meanwhile, the permanent viscosity η_v approached its upper bound for all specimens, implying that the viscous flow term contributed only marginally to long-term deformation of CLT and CLBT. These findings confirm that bamboo reinforcement effectively improves the time-dependent performance of laminated composites.
7. Implemented via `InitStrainMaterial` in OpenSeesPy, the calibrated creep produced a gradual reduction of mid-span bending moments and a modest increase of end moments in a CLBT-supported beam, i.e., a shift of demand towards the restraints over time. Daily survival probabilities evaluated by Monte Carlo and FORM evidenced a small but measurable reduction in reliability that stabilizes as the Kelvin branch saturates.

The design implications are: (*i*) Climate sensitivity should be explicit in serviceability assessments of CLT and CLBT, with creep checks carried out under representative temperature and humidity histories; (*ii*) unloaded control elements (or in-situ monitoring) are valuable for filtering hygrothermal strains; (*iii*) for indeterminate systems, progressive moment redistribution towards supports motivates detailing and verification of end regions for long-term effects; (*iv*) probabilistic, climate-aware creep models provide decision-grade demand envelopes and are readily integrated in standard FE workflows.

The present calibration is limited to the tested layups and a 180-day horizon under the recorded laboratory climate conditions; for longer service lives extending to several decades—as typically required in structural design—extrapolation can be performed using the calibrated Burgers model, in which the viscous flow term (governed by η_v) primarily controls the long-term permanent deformation while the

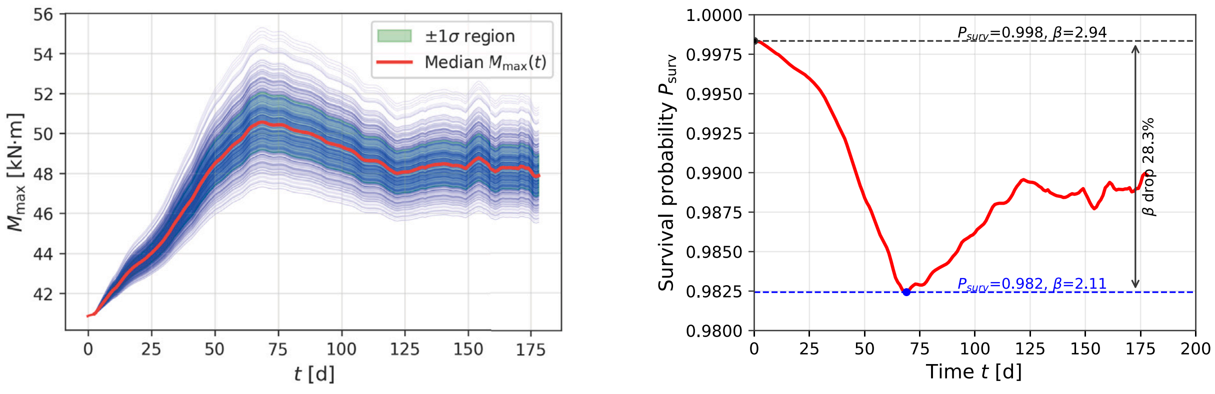

(a) (b)

Fig. 15. Probabilistic assessment under column creep: (a) ensemble of $M_{\max}(t)$ trajectories from Monte Carlo simulation ($N = 500$); (b) daily survival probability $P_{\mathrm{surv}}(t) = 1 - P_{\mathrm{f}}(t)$.

Table A.1
Linear regression parameters (a and b) describing the correlation between vertical creep strain and environmental factors (temperature T and absolute humidity AH) for different material types. The last two columns summarize the mean value and the coefficient of variation (COV) of each parameter across all test groups.

Factor	Parameter	Specimen group						Statistical summary	
		CLT-C30	CLT-C15	CLBT1-C30	CLBT1-C15	CLBT2-C30	CLBT2-C15	Mean	COV (%)
T	a	-1.98×10^{-3}	-3.40×10^{-4}	-1.21×10^{-3}	-5.93×10^{-4}	-2.30×10^{-3}	-1.92×10^{-3}	-1.39×10^{-3}	57.90
	b	0.27	0.13	0.17	0.10	0.27	0.19	0.19	37.00
AH	a	6.44×10^{-4}	-1.09×10^{-3}	-1.10×10^{-3}	-1.65×10^{-3}	8.54×10^{-4}	-1.64×10^{-3}	-6.64×10^{-4}	169.00
	b	0.23	0.13	0.16	0.10	0.22	0.17	0.17	29.40

Table B.2
Posterior statistics and pairwise correlations for CLT. Columns report the posterior mean, standard deviation (Stand. dev.), and the 3% and 97% Highest Density Intervals (HDI). The right block lists pairwise correlation coefficients (upper triangular).

Parameter	Mean	Stand. dev.	HDI 3%	HDI 97%	Correlation coefficients (upper triangular)						
					E_{e}	E_{d}	η_{d}	η_{v}	h_2	h_5	σ
E_{e}	8160.8	266.92	7638.6	8651.5	1	−0.5048	−0.8753	−0.0049	0.5847	−0.2169	−0.0225
E_{d}	3038.3	36.99	2973.4	3108.8	–	1	0.2115	−0.1445	−0.1085	−0.0062	0.0102
η_{d}	1.06×10^{5}	5.36×10^{3}	9.59×10^{4}	1.16×10^{5}	–	–	1	0.0310	−0.6872	0.3009	0.0224
η_{v}	5.15×10^{8}	2.80×10^{8}	8.64×10^{7}	9.93×10^{8}	–	–	–	1	0.0041	0.0212	0.0032
h_2	−0.0474	0.00838	−0.0645	−0.0333	–	–	–	–	1	−0.6840	0.0002
h_5	0.0219	0.00635	0.00987	0.0335	–	–	–	–	–	1	−0.0008
σ	0.1040	0.00329	0.0977	0.1102	–	–	–	–	–	–	1

Table B.3
Posterior statistics and pairwise correlations for CLBT1. Columns report the posterior mean, standard deviation (Stand. dev.), and the 3% and 97% Highest Density Intervals (HDI). The right block lists pairwise correlation coefficients (upper triangular).

Parameter	Mean	Stand. dev.	HDI 3%	HDI 97%	Correlation coefficients (upper triangular)						
					E_{e}	E_{d}	η_{d}	η_{v}	θ_7	θ_8	σ
E_{e}	7861.19	250.13	7400.12	8342.60	1	−0.6438	−0.7348	0.0215	−0.2014	0.0955	0.0342
E_{d}	13 019.9	994.77	11 225.7	14 941.5	–	1	0.0837	−0.1742	0.3577	−0.6755	−0.0305
η_{d}	2.27×10^{5}	3.83×10^{4}	1.54×10^{5}	2.97×10^{5}	–	–	1	0.0523	0.0686	0.3341	−0.0188
η_{v}	4.83×10^{8}	2.87×10^{8}	1.09×10^{7}	9.32×10^{8}	–	–	–	1	−0.0656	0.0620	0.00095
θ_7	0.00437	0.00058	0.00321	0.00541	–	–	–	–	1	−0.7058	−0.0342
θ_8	−0.00516	0.00095	−0.00714	−0.00353	–	–	–	–	–	1	0.0261
σ	0.1165	0.00350	0.1101	0.1230	–	–	–	–	–	–	1

probabilistic hygrothermal correction terms account for cumulative temperature and humidity exposure over extended periods. Additionally, all tests were conducted under sustained uniaxial compression, a loading condition directly relevant to vertical load-bearing elements such as columns and walls in mid- to high-rise buildings; however, the results cannot be directly generalized to bending-dominated members, tension-dominated states, horizontal (transverse) creep, or multi-axial stress conditions without additional experimental validation and potential refinement of the mechano-sorptive constitutive relations. Future work should address (*i*) longer monitoring windows and diverse climatic conditions; (*ii*) other species, adhesives, and lamination patterns; (*iii*) coupled moisture transport and advanced mechano-sorptive constitutive laws; and (*iv*) broader reliability studies on full-scale assemblies. Ultimately, incorporating climate-aware, probabilistic creep provisions

Table B.4
Posterior statistics and pairwise correlations for CLBT2. Columns report the posterior mean, standard deviation (Stand. dev.), and the 3% and 97% Highest Density Intervals (HDI). The right block lists pairwise correlation coefficients (upper triangular).

Parameter	Mean	Stand. dev.	HDI 3%	HDI 97%	Correlation coefficients (upper triangular)						
					E_e	E_d	η_d	η_v	θ_7	θ_8	σ
E_e	7921.18	306.33	7394.16	8527.22	1	−0.4335	−0.8183	−0.0183	−0.3694	0.5237	−0.0554
E_d	4825.43	290.56	4230.83	5301.39	–	1	0.0323	−0.1275	−0.1362	−0.5462	−0.0203
η_d	2.15×10^5	1.99×10^4	1.79×10^5	2.52×10^5	–	–	1	0.0409	0.5933	−0.4763	0.0854
η_v	5.01×10^8	2.94×10^8	5.38×10^6	9.44×10^8	–	–	–	1	0.0202	0.0098	0.0450
θ_7	0.00799	0.00092	0.00622	0.00971	–	–	–	–	1	−0.6806	0.0567
θ_8	−0.00986	0.00107	−0.0118	−0.00739	–	–	–	–	–	1	−0.0421
σ	0.15447	0.00478	0.1446	0.1629	–	–	–	–	–	–	1

into design guidance would support performance-based criteria for CLT and hybrid bamboo-timber structures.

CRediT authorship contribution statement

Zeda Yang: Writing – review & editing, Writing – original draft, Investigation, Data curation, Conceptualization. **Hanlin Wei:** Writing – review & editing, Writing – original draft, Software, Investigation, Formal analysis. **Vittoria Borghese:** Writing – review & editing, Formal analysis. **Marco Zucca:** Writing – review & editing, Formal analysis. **Flavio Stochino:** Writing – review & editing, Supervision, Methodology, Investigation. **Yan Xiao:** Writing – review & editing, Supervision, Project administration, Funding acquisition. **Cristoforo Demartino:** Writing – review & editing, Supervision, Project administration, Methodology, Investigation, Funding acquisition.

Declaration of competing interest

The authors declare that they have no known competing financial interests or personal relationships that could have appeared to influence the work reported in this paper.

Acknowledgements

Funding for this research was provided by the National Natural Science Foundation of China (Project 51978606) and the European Union – Next Generation EU (AI-ENVISERS project, PRIN 2022 PNRR programme, D.D.1409 del 14/09/2022 Ministero dell'Università e della Ricerca). This manuscript reflects only the authors' views and opinions, and the Ministry cannot be considered responsible for them.

Appendix A. Fitted regression parameters for the correlation between creep strain and hygrothermal factors

This appendix provides the detailed linear regression parameters (a and b) derived from the correlation analysis presented in Section 3.2.2. These parameters quantify the sensitivity of the vertical creep strain (measured from day 60 onwards) to variations in ambient temperature (T) and absolute humidity (AH).

Appendix B. Posterior statistics and pairwise correlations

This appendix presents the complete posterior statistics for the probabilistic creep models calibrated in Section 4.2. For each material type (CLT, CLBT1, and CLBT2), the following tables list the posterior mean, standard deviation, and the 3% and 97% Highest Density Intervals (HDI) for the model parameters. Additionally, the pairwise correlation coefficients are provided to illustrate the interdependence between the parameters.

Data availability

Data will be made available on request.

References

[1] M.H. Ramage, H. Burridge, M. Busse-Wicher, G. Fereday, T. Reynolds, D.U. Shah, G. Wu, L. Yu, P. Fleming, D. Densley-Tingley, et al., The wood from the trees: The use of timber in construction, Renew. Sustain. Energy Rev. 68 (2017) 333–359.

[2] R. Jockwer, P. Grönquist, A. Frangi, Long-term deformation behaviour of timber columns: Monitoring of a tall timber building in Switzerland, Eng. Struct. 234 (2021) 111855.

[3] Y. Xiao, J. Li, L. Deng, H. Li, Q. Zhang, Research progress of cross-laminated timber and bamboo (CLTB) (in Chinese), J. Build. Struct. 43 (1) (2022) 1–19.

[4] H.F. Archila, A. Rhead, M.P. Ansell, P. Walker, J. Lizarazo-Marriaga, Elastic response of cross-laminated engineered bamboo panels subjected to in-plane loading, Proc. Inst. Civ. Eng.-Constr. Mater. 172 (6) (2019) 284–295.

[5] Y. Xiao, H. Cai, S. Dong, A pilot study on cross-laminated bamboo and timber beams, J. Struct. Eng.-ASCE 147 (2021) 06021002.

[6] X. Luo, X. Wang, H. Ren, S. Zhang, Y. Zhong, Long-term mechanical properties of bamboo scrimber, Constr. Build. Mater. 338 (2022) 127659.

[7] J. Gottron, K.A. Harries, Q. Xu, Creep behaviour of bamboo, Constr. Build. Mater. 66 (2014) 79–88.

[8] H. Zanker, A. Rajabipour, D. Huang, M. Bazli, S. Tang, Z. Cui, J. Zhu, J. Kennaway, L.H. Diaz, Creep analysis of bamboo composite for structural applications, Polymers 15 (3) (2023).

[9] J. Porteous, A. Kermani, EC5 - deformation and creep of timber structures, Struct. Eng. 87 (17) (2009) 25–29.

[10] M. Fragiacomo, M.L. Batchelar, Timber frame moment joints with glued-in steel rods. II: Experimental investigation of long-term performance, J. Struct. Eng. 138 (6) (2012) 802–811.

[11] M. Derikvand, N.J. Kotlarewski, M. Lee, H. Jiao, A.H.C. Chan, G. Nolan, Short-term and long-term bending properties of nail-laminated timber constructed of fast-grown plantation eucalypt, Constr. Build. Mater. 211 (2019) 952–964.

[12] F. Dubois, J. Dopeux, O. Pop, M. Metrope, Long-term creep behavior of timber columns: Experimental and numerical protocols, Eng. Struct. 275 (2023) 115283.

[13] S. Wu, K. Tong, J. Wang, Y. Li, Experimental and analytical study on creep characteristics of box section bamboo-steel composite columns under long-term loading, Materials 14 (4) (2021) 983.

[14] Y. Liu, W. Jia, X. Su, H. Ma, Z. Xiao, Assessing the creep performance of full-scale bamboo scrimber columns, BioResources 16 (2) (2021) 3691–3707.

[15] J. Zhang, K. Tong, Q. Shan, Y. Li, Examining mechanical behavior of steel-bamboo composite I-section column under long-term loading, J. Build. Eng. 45 (2022).

[16] X. Ma, S.Q. Shi, G. Wang, B. Fei, Z. Jiang, Long creep-recovery behavior of bamboo-based products, J. Wood Sci. 64 (2) (2018) 119–125.

[17] Y. Wei, K. Zhao, C. Hang, S. Chen, M. Ding, Experimental study on the creep behavior of recombinant bamboo, J. Renew. Mater. 8 (3) (2020) 251–273.

[18] Y. Xiao, L. Li, R.Z. Yang, Long-term loading behavior of a full-scale glubam bridge model, J. Bridg. Eng. 19 (9) (2014) 04014027.1–04014027.7.

[19] D.G. Hunt, J. Gril, Evidence of a physical ageing phenomenon in wood, J. Mater. Sci. Lett. 15 (1) (1996) 80–82.

[20] A. Hanhijärvi, Advances in the knowledge of the influence of moisture changes on the long-term mechanical performance of timber structures, Mater. Struct./Mater. Constr. 33 (1) (2000) 43–49.

[21] A. Hermawan, H. Sakagami, N. Fujimoto, Creep behaviour of Japanese cypress timber under various hygrothermal conditions, Wood Mater. Sci. Eng. 17 (3) (2022) 221–229.

[22] Y. Huang, Creep behavior of wood under cyclic moisture changes: interaction between load effect and moisture effect, J. Wood Sci. 62 (5) (2016) 392–399.

[23] C. Montero, J. Gril, C. Legeas, D.G. Hunt, B. Clair, Influence of hygromechanical history on the longitudinal mechanosorptive creep of wood, Holzforschung 66 (6) (2012) 757–764.

[24] J.S. Stevanic, L. Salmeń, Molecular origin of mechano-sorptive creep in cellulosic fibres, Carbohydr. Polymers 230 (2020) 115615.

[25] P. Navi, V.E. Pittet, C.J.G. Plummer, Transient moisture effects on wood creep, Wood Sci. Technol. 36 (6) (2002) 447–462.

[26] T. Tsubaki, T. Nakano, Creep behavior of bamboo under various desorption conditions, Holzforschung 64 (4) (2010) 489–493.

[27] X. Ma, Z. Luo, C.H. Ji, L. Cai, B. Fei, Flexural creep behaviors of bamboo subjected to different gradient variation directions and relative humidity, Ind. Crop. Prod. (2022).

[28] H. Pearson, S. Ormarsson, B.L. Gabbitas, Nonlinear tensile creep behavior of radiata pine at elevated temperatures and different moisture contents, Holzforschung 69 (7) (2015) 915–923.

[29] T. Hsieh, F.-C. Chang, Effects of moisture content and temperature on wood creep, Holzforschung 72 (12) (2018) 1071–1078.

[30] F. Xi, L. Zhao, Y. Wei, J. Yi, K. Zhao, Effect of temperature on the bending and creep properties of wood plastic composites, Polym. Compos. 44 (8) (2023) 4612–4622.

[31] L. Liu, Y. Zhang, C. Sun, H. Li, L. Ma, Insights into wood species and aging effects on pyrolysis characteristics and combustion model by multi kinetics methods and model constructions, Energies 16 (4) (2023) 1563.

[32] C. Liu, X. Wu, X. Liu, X. Li, Z. Chen, H. Luo, Study of creep behavior and a viscoelastic model of bamboo scrimber under short-term parallel-to-grain compression, J. Mater. Civ. Eng. (2024).

[33] M.K. Habibi, L.-H. Tam, D. Lau, Y. Lu, Viscoelastic damping behavior of structural bamboo material and its microstructural origins, Mech. Mater. 97 (2016) 44–52.

[34] K. Ando, R. Nakamura, T. Kushino, Variation of shear creep properties of wood within a stem: effects of macro- and microstructural variability, Wood Sci. Technol. 57 (1) (2023) 93–110.

[35] S. Cai, Y. Guo, Y. Li, Intratree variation in viscoelastic properties of cell walls of masson pine (Pinus massoniana lamb), J. Renew. Mater. 10 (1) (2022) 119–133.

[36] N.W. Tschoegl, The Phenomenological Theory of Linear Viscoelastic Behavior: an Introduction, Springer Science & Business Media, 2012.

[37] W.N. Findley, F.A. Davis, Creep and Relaxation of Nonlinear Viscoelastic Materials, Courier corporation, 2013.

[38] R.M. Christensen, Theory of Viscoelasticity, Courier Corporation, 2013.

[39] L.C. Nguedjio, J.M. Takam, R.M. Pitti, B. Blaysat, N. Sauvat, J. Gril, F. Zemtchou, P. Talla, Analyzing creep-recovery behavior of tropical Entandrophragma cylindricum wood: Traditional and fractional modeling methods, Int. J. Solids Struct. 306 (2025) 113122.

[40] M.F. Sá, A.M. Gomes, J.R. Correia, N. Silvestre, Creep behavior of pultruded GFRP elements–part 1: Literature review and experimental study, Compos. Struct. 93 (10) (2011) 2450–2459.

[41] T.B. Ratanawilai, V. Leelasilapasart, C. Srivabut, S.B. Ratanawilai, Lifetime prediction under dead-load long-term creep test and models analysis of wood-plastic composites for building materials, Plast. Rubber Compos. 52 (9) (2023) 506–515.

[42] M.A.A. Alrubaie, D.J.S. Gardner, R.A. Lopez-Anido, Modeling the long-term deformation of a geodesic spherical frame structure made fromwood plastic composite lumber, Appl. Sci. (Switzerland) 10 (14) (2020) 5017.

[43] W.B. Luo, C.H. Wang, R.G. Zhao, Application of time-temperature-stress superposition principle to nonlinear creep of poly (methyl methacrylate), Key Eng. Mater. 340 (2007) 1091–1096.

[44] D.A. Souto-Silvar, A. Álvarez-García, A. Díaz-Díaz, F.J. Rodríguez-Dopico, J. López-Beceiro, Application of the time–temperature superposition principle to predict long-term behaviour of an adhesive for use in shipbuilding, Arab. J. Sci. Eng. 49 (2) (2024) 2345–2355.

[45] J. Greenwood, D. Young, Measuring creep of drainage materials by means of the stepped isothermal method in compression, in: Paper 221 Proceedings Eurogeo, 2008.

[46] I.P. Giannopoulos, C.J. Burgoyne, Prediction of the long-term behaviour of high modulus fibres using the stepped isostress method (SSM), J. Mater. Sci. 46 (24) (2011) 7660–7671.

[47] S.T. Akter, E. Binder, T.K. Bader, Moisture and short-term time-dependent behavior of Norway spruce clear wood under compression perpendicular to the grain and rolling shear, Wood Mater. Sci. Eng. 18 (2) (2023) 580–593.

[48] Y. Saadallah, S. Flilissa, B. Hamadouche, Viscoelastic creep in bending of olive wood (Olea Europea L.), J. Indian Acad. Wood Sci. 21 (1) (2024) 58–64.

[49] K. Shimazaki, K. Ando, Analysis of shear creep behaviors of hardwood and softwood using creep recovery curves, Eur. J. Wood Wood Prod. 83 (4) (2025) 1–12.

[50] S. Xu, Z. He, J. Xu, J. Zhang, Y. Cao, P. Yang, X. Zhou, Q. Wu, Low-temperature plasma treatment as a facile, low-cost, and efficient methodology to improve the creep resistance of laminated veneer lumber, Wood Mater. Sci. Eng. (2025).

[51] R. Li, A. Chen, L. Yang, G. He, H. Wang, Experimental study on long-term performance of simply-supported glulam beams connected with steel joining plates and bolts, in: Structures, vol. 73, Elsevier, 2025, 108439.

[52] N. Guo, Y. Zhang, L. Mei, Y. Zhao, Experimental study on flexural performance of the prestressed glulam continuous beam after long-term loading, Buildings 12 (7) (2022) 895.

[53] Y. Xiao, R. Yang, B. Shan, Production, environmental impact and mechanical properties of glubam, Constr. Build. Mater. 44 (2013) 765–773.

[54] A.M. Hubbard, K.E. Copenhaver, C.M. Clarkson, A.E. Marquez-Rossy, M.L. Rencheck, M.E. Lamm, S. Ozcan, Creep suppression and fatigue in bio-based composites manufactured via conventional and large format additive manufacturing processes, Next Mater. 9 (2025).

[55] A. Yang, Z. Liao, Z. Xu, T. Liu, Y. Fang, W. Wang, M. Xu, Y. Song, Q. Wang, Y. Li, Scalable production of robust and creep resistant ultra-high filled wood-plastic composites, Compos. B 289 (2025).

[56] X. Ye, Y. Ye, Y. Han, F. Ren, H. Ma, W. Xu, Z. Zhou, Bamboo powders effectively reinforcing the modulus of PBAT composites and creep resistance, Polym. Eng. Sci. 64 (12) (2024) 6088–6098.

[57] M. Fragiacomo, A. Ceccotti, Long-term behavior of timber-concrete composite beams. I: Finite element modeling and validation, J. Struct. Eng. 132 (1) (2006) 13–22.

[58] D. Honfi, Time-variant reliability of timber beams according to eurocodes considering long-term deflections, Wood Mater. Sci. Eng. 15 (5) (2020) 250–260.

[59] D.V. Rosowsky, W.M. Bulleit, Another look at load duration effects in wood, J. Struct. Eng. 128 (6) (2002) 824–828.

[60] J. Köhler, J.D. Sørensen, M.H. Faber, Probabilistic modeling of timber structures, Struct. Saf. 29 (4) (2007) 255–267.

[61] M.H. Faber, J. Köhler, J.D. Sorensen, Probabilistic modeling of graded timber material properties, Struct. Saf. 26 (3) (2004) 295–309.

[62] J. Kohler, S. Svensson, Probabilistic representation of duration of load effects in timber structures, Eng. Struct. 33 (2) (2011) 462–467.

[63] D. Honfi, A. Mårtensson, S. Thelandersson, R. Kliger, Modelling of bending creep of low-and high-temperature-dried spruce timber, Wood Sci. Technol. 48 (1) (2014) 23–36.

[64] P. Gardoni, A. Der Kiureghian, K.M. Mosalam, Probabilistic capacity models and fragility estimates for reinforced concrete columns based on experimental observations, J. Eng. Mech. 128 (10) (2002) 1024–1038.

[65] Joint Committee on Structural Safety (JCSS), JCSS Probabilistic Model Code – Part 3: Resistance Models, Technical Report, Joint Committee on Structural Safety, Zurich, Switzerland, 2010.

[66] A. Bonfanti, J.L. Kaplan, G. Charras, A. Kabla, Fractional viscoelastic models for power-law materials, Soft Matter 16 (26) (2020) 6002–6020.

[67] S. Sun, M. Wan, Evaluation of the applicability of different viscoelasticity constitutive models in bamboo scrimber short-term tensile creep property research, Sci. Eng. Compos. Mater. 28 (1) (2021) 363–371.

[68] G.E. Box, G.C. Tiao, Bayesian Inference in Statistical Analysis, John Wiley & Sons, 2011.

[69] Standardization Administration of China, GB/T 50329-2012: Standard for Test Methods of Timber Structures, 2012, National Standard of the People's Republic of China (in Chinese).

[70] European Committee for Standardization (CEN), BS EN 408:2010 timber structures. Structural timber and glued laminated timber. Determination of some physical and mechanical properties, 2010, British Standards Institution (BSI).

[71] H. Wei, D. Shi, E. Rupert, M. Fragiacomo, C. Demartino, Y. Xiao, Axial compressive behavior of novel laminated bamboo tubes: Experimental tests and predictive buckling model, Constr. Build. Mater. 463 (2025) 139987.

[72] K. Naumenko, H. Altenbach, Modeling of Creep for Structural Analysis, Springer, 2007.

[73] J. Betten, Creep Mechanics, Springer, 2005.

[74] J. Kim, G.A. Sholar, S. Kim, Determination of accurate creep compliance and relaxation modulus at a single temperature for viscoelastic solids, J. Mater. Civ. Eng. 20 (2) (2008) 147–156.

[75] X. Sun, M. He, Z. Li, J. Ou, X. Zheng, M. Wei, Experimental study on the long-term creep behavior of cross-laminated timber under axial compression used for mass timber structural systems, Eng. Struct. 338 (2025) 120644.

[76] X. Zheng, Z. Li, M. He, F. Lam, Experimental investigation on the rheological behavior of timber in longitudinal and transverse compression, Constr. Build. Mater. 304 (2021) 124633.

[77] T.T. Nguyen, T.N. Dao, S. Aaleti, K. Hossain, K.J. Fridley, Numerical model for creep behavior of axially loaded CLT panels, J. Struct. Eng. 145 (1) (2019) 04018224.

[78] H. Li, L. Wang, Y. Wei, B.J. Wang, Off-axis compressive behavior of cross-laminated bamboo and timber wall elements, in: Structures, vol. 35, Elsevier, 2022, pp. 452–468.

[79] H. Li, Y. Wei, L. Yan, K.E. Semple, C. Dai, In-plane compressive behavior of short cross-laminated bamboo and timber, Ind. Crop. Prod. 200 (2023) 116807.

[80] P. Morlier, Creep in Timber Structures, CRC Press, 1994.

[81] J. Dinwoodie, J.-A. Higgins, B. Paxton, D. Robson, Creep research on particleboard: 15 year's work at the UK building research establishment, Holz Als Roh-Und Werkst. 48 (1) (1990) 5–10.

[82] M. Yahyaei-Moayyed, F. Taheri, Experimental and computational investigations into creep response of AFRP reinforced timber beams, Compos. Struct. 93 (2) (2011) 616–628.

[83] European Committee for Standardization (CEN), Wood-based panels – determination of duration of load and creep factors, 2013, European Standard EN 1156:2013.

[84] A.-M. Olsson, L. Salmén, M. Eder, I. Burgert, Mechano-sorptive creep in wood fibres, Wood Sci. Technol. 41 (1) (2007) 59–67.

[85] J. Strömbro, P. Gudmundson, Mechano-sorptive creep under compressive loading–A micromechanical model, Int. J. Solids Struct. 45 (9) (2008) 2420–2450.

[86] A. Ranta-Maunus, The viscoelasticity of wood at varying moisture content, Wood Sci. Technol. 9 (3) (1975) 189–205.

[87] P. Hoffmeyer, R. Davidson, Mechano-sorptive creep mechanism of wood in compression and bending, Wood Sci. Technol. 23 (3) (1989) 215–227.

[88] C.C. Gerhards, Effect of moisture content and temperature on the mechanical properties of wood: an analysis of immediate effects, Wood Fiber Sci. (1982) 4–36.

[89] M. Zhu, F. McKenna, M.H. Scott, OpenSeesPy: Python library for the OpenSees finite element framework, SoftwareX 7 (2018) 6–11.